Monthly Notices of the ROYAL ASTRONOMICAL SOCIETY

MNRAS **545,** 1–19 (2026) https://doi.org/10.1093/mnras/staf1965
Advance Access publication 2025 November 11

Ultraviolet spectroscopy of the black hole X-ray binary MAXI J1820+070 across a state transition

M. Georganti [1]★ C. Knigge [1] N. Castro Segura [1,2] K. S. Long,[3,4] G. C. Dewangan [5] S. Banerjee,[5] R. I. Hynes,[6] P. Gandhi [1] D. Altamirano,[1] J. Patterson[7] and D. R. Zurek[8]

[1]*School of Physics and Astronomy, University of Southampton, Southampton, Hampshire SO17 1BJ, UK*
[2]*Department of Physics, University of Warwick, Coventry CV4 7AL, UK*
[3]*Space Telescope Science Institute, 3700 San Martin Drive, Baltimore, MD 21218, USA*
[4]*Eureka Scientific Inc., 2452 Delmer Street, Suite 100, Oakland, CA 94602-3017, USA*
[5]*Inter-University Centre for Astronomy and Astrophysics (IUCAA), Ganeshkhind, Pune 411007, India*
[6]*Department of Physics and Astronomy, Louisiana State University, Baton Rouge, LA 70803, USA*
[7]*Department of Astronomy, Columbia University, 538 West & 120th Street, New York, NY 10027, USA*
[8]*Department of Astrophysics, American Museum of Natural History, CPW & 79th street, New York, NY 10024-5192, USA*

Accepted 2025 October 1. Received 2025 September 15; in original form 2025 January 21

ABSTRACT

We present ultraviolet (UV) spectroscopic observations covering three distinct accretion states of the low-mass X-ray binary (LMXB) MAXI J1820+070: the luminous hard state, a hard-intermediate state, and the soft state. Our observations were obtained during the 2018 outburst of MAXI J1820+070 with the *Hubble Space Telescope* (*HST*) and *AstroSat* observatory. The extinction towards the source turns out to be low – $E_{B-V} = 0.20 \pm 0.05$ – making it one of the best UV accretion laboratories among LMXBs. Remarkably, we observe only moderate differences between all three states, with all spectra displaying similar continuum shapes and emission lines. Moreover, the continua are not well-described by physically plausible irradiated disc models. All of this challenges the standard reprocessing picture for UV emission from erupting LMXBs. The UV emission lines are double-peaked, with high-ionization lines displaying higher peak-to-peak velocities. None of the lines displays obvious outflow signatures, even though blue-shifted absorption features have been seen in optical and near-infrared lines during the hard state. The emission line ratios are consistent with normal abundances, suggesting that the initial donor mass was low enough to avoid CNO processing ($M_{2,i} \lesssim 1.0$–$1.5\,M_\odot$). Finally, we study the evolution of UV variability in our time-resolved *HST* observations (hard and hard-intermediate states). All UV power spectra can be modelled with a broken power law, superposed on which we tentatively detect the $\simeq 18$ s quasi-periodic oscillation that has been seen in other spectral bands.

Key words: accretion, accretion discs – stars: black holes – stars: individual: MAXI J1820+070 – X-rays: binaries.

1 INTRODUCTION

MAXI J1820+070 (= ASASSN-18ey) is one of the closest, brightest and least-reddened Galactic black hole X-ray transients (BHXTs). It was discovered after its outburst onset on 2018 March (M. A. Tucker et al. 2018; T. Kawamuro et al. 2018). Since it is an excellent target for studying black hole (BH) accretion, unprecedented monitoring has been carried out across the entire electromagnetic spectrum, covering the main outburst of the source and the subsequent reflaring episodes (e.g. M. C. Baglio, D. M. Russell & F. Lewis 2018; P. Atri et al. 2020; H. Stiele & A. K. H. Kong 2020; A. J. Tetarenko et al. 2021b; M. Özbey Arabacı et al. 2022; T. Yoshitake et al. 2022; S. Banerjee et al. 2024).

During canonical outbursts, BHXTs typically follow the same evolutionary track and cycle between two distinctive X-ray states, the *hard* and the *soft* state. The outburst evolution is hysteretic: in the *hardness–intensity diagram* (HID; e.g. see R. P. Fender, T. M. Belloni & E. Gallo 2004, for more information), where the spectral hardness of the accretion flow is plotted against the X-ray luminosity, erupting BHXTs trace a '*q*-shaped' path. The geometry of the accretion flow, the X-ray spectrum and the variability properties are all strongly *state-dependent* (e.g. A. A. Esin, J. E. McClintock & R. Narayan 1997; J. Homan et al. 2001; A. A. Zdziarski & M. Gierliński 2004; J. Homan & T. Belloni 2005; R. A. Remillard & McClintock 2006; C. Done, M. Gierliński & A. Kubota 2007; T. M. Belloni 2010; M. Gilfanov 2010; T. M. Belloni & S. E. Motta 2016 and references therein).

At the beginning and end of an outburst, the system is in the hard state. In this state, the inner edge of the geometrically thin accretion disc is located far from the BH. The broad-band spectral energy distribution (SED) is then dominated by a hard (power law, $\Gamma < 2$, high-energy cut-off around 100 keV) component, which is the result of low-energy photons being upscattered by relativistic electrons in a hot 'corona'. A weak thermal component associated with the accretion disc may also be apparent in lower energies (J. E.

★ E-mail: m.georganti@outlook.com

Grove et al. 1998). Timing observations tend to show strong X-ray variability – of the order of 20–50 per cent (e.g. T. Belloni et al. 2005; T. Muñoz-Darias, S. Motta & T. M. Belloni 2011; T. M. Belloni & L. Stella 2014; S. E. Motta 2016) – while the power density spectra (PDS) are characterized by red noise, low-frequency breaks, and often, quasi-periodic oscillations (QPOs). The latter are mostly seen in the low-frequency regime (0.01–30 Hz) and commonly associated with either geometrical effects such as the Lense–Thirring precession of the hot accretion flow in the vicinity of the BH (L. Stella & M. Vietri 1998; L. Stella, M. Vietri & S. M. Morsink 1999; J. D. Schnittman, J. Homan & J. M. Miller 2006; A. Ingram, C. Done & P. C. Fragile 2009; A. R. Ingram & S. E. Motta 2019), instabilities such as the accretion/jet instability (M. Tagger & R. Pellat 1999; P. Varnière, J. Rodriguez & M. Tagger 2002; P. Varnière, M. Tagger & J. Rodriguez 2012; J. Ferreira et al. 2022), or coronae oscillations (L. Titarchuk & R. Fiorito 2004; C. Cabanac et al. 2010). At radio and infrared wavelengths, collimated, relativistic jets are also commonly observed in this state (e.g. S. Markoff, H. Falcke & R. Fender 2001; S. Corbel et al. 2003; R. P. Fender et al. 2004; R. P. Fender, J. Homan & T. M. Belloni 2009; R. Fender & E. Gallo 2014).

As the source brightens and the edge of the inner disc moves towards the innermost stable circular orbit (ISCO) of the BH, the system proceeds to the *soft* state. Notable changes occur in the X-ray spectrum. The hard component becomes softer ($\Gamma > 2$) but characteristically extends in a coronal tail exceeding 500 keV associated with the faint Comptonization region (e.g. T. M. Belloni & S. E. Motta 2016) while the SED is dominated by the soft thermal component associated with the geometrically thin, optically thick accretion disc (N. Shakura & R. Sunyaev 1973). Variability during the soft state is limited to amplitudes of a few per cent (commonly between 1 per cent and 5 per cent; e.g. P. Casella et al. 2004; T. Belloni et al. 2005; T. Muñoz-Darias et al. 2011; T. M. Belloni & L. Stella 2014; S. E. Motta 2016), while the PDS are described by a weaker, broken power-law component. QPOs are also sometimes present, but they are broader and weaker than the ones found in the hard state. They are plausibly associated with the accretion/jet instability (P. Varnière et al. 2002, 2012) or the launch of the relativistic jet away from the system (R. P. Fender et al. 2009). Radio emission is quenched in the soft state (e.g. R. Fender et al. 1999, 2004, 2009; S. Corbel et al. 2001; J. M. Miller et al. 2008; D. M. Russell et al. 2011), but blue-shifted X-ray absorption lines associated with highly ionized disc winds often emerge (e.g. J. M. Miller et al. 2006b, 2008; J. Neilsen & J. C. Lee 2009; G. Ponti, T. Muñoz-Darias & R. P. Fender 2014; M. Díaz Trigo & L. Boirin 2016; G. Ponti et al. 2016; N. Higginbottom et al. 2018), preferentially seen in high-inclination (G. Ponti et al. 2012) and sub-Eddington luminosity (N. Higginbottom et al. 2019, 2020) systems. The transitions between hard and soft states proceed via *intermediate* states, which can arise at different luminosities due to the hysteretic nature of the eruptions. However, these transitional states are more difficult to study and can present complex signatures during their brief window of occurrence.

1.1 The ultraviolet window into accretion

A significant challenge for the study of BHXTs is that interstellar extinction usually prevents us from exploring the ultraviolet (UV) response to changes in X-ray luminosity and state transitions. This is unfortunate, as the UV band is a critical link between the inner accretion flow (the corona and the hot, viscously dominated disc) and the outer one (the cool, irradiation-dominated disc). To date, only six BHXTs have been observed in the far-UV part of the spectrum near outburst peak in the soft state (R. I. Hynes 2005). Increasing the size of this sample is important for understanding how the disc evolves and responds to the changing X-ray irradiation during eruptions, what drives the presence of disc wind signatures in specific wavelengths during different states (e.g. T. Muñoz-Darias et al. 2016, 2019; T. Muñoz-Darias, M. A. P. Torres & M. R. Garcia 2018; J. Sánchez-Sierras & T. Muñoz-Darias 2020; N. Castro Segura et al. 2022; S. Fijma et al. 2023), and to shed light on the periodic and aperiodic variability produced at intermediate disc radii. MAXI J1820+070 provides us with a rare opportunity to make progress in this area. Here, we present the first multi-epoch UV characterization of a BHXT across both outburst states, which allows us to shed light on some of these issues.

The outbursts of BHXTs are typically interpreted in the context of the *disc instability model* (DIM; e.g. J. Lasota 2001; J. M. Hameury 2020 for a recent review), according to which the accretion discs in these systems are subject to a thermal-viscous instability related to the ionization of hydrogen. To what extent X-ray irradiation plays a significant role in controlling the behaviour of the discs in BHXTs is still a matter of debate (e.g. J. van Paradijs & J. E. McClintock 1994; J. van Paradijs 1996; A. R. King & H. Ritter 1998; G. Dubus et al. 1999; G. Dubus, J. M. Hameury & J. P. Lasota 2001; B. E. Tetarenko et al. 2018a). Strongly irradiated accretion discs are needed, though, to explain the longer and brighter eruptions of these systems and their light curve phenomenology. The outer disc is heated by radiation emitted in the inner regions, which keeps it ionized and prevents an early return to quiescence. It also means that the outer disc produces most of the UV/optical, and sometimes infrared, flux. This picture can be tested by modelling the UV SED with irradiated disc models.

The spectral lines seen in the UV also provide important diagnostics. For example, the He II λ1640 recombination line is an effective bolometer for the (usually unobservable) extreme UV (EUV) band above 54 eV. Moreover, UV line *ratios* can be used to shed light on the evolutionary history of the binary, since they strongly depend on the degree of CNO processing the accreting material has been subjected to (e.g. C. W. Mauche, Y. P. Lee & T. R. Kallman 1997; C. A. Haswell et al. 2002; B. T. Gänsicke et al. 2003; C. S. Froning et al. 2011, 2014; N. Castro Segura et al. 2024, for both the cases of cataclysmic variables, CVs, and LMXBs). Perhaps most importantly, however, the strong UV resonance lines (N V λ1240, Si IV λ1400, C IV λ1550) are highly sensitive outflow tracers.

The observable wind signatures presented by spectral lines take the form of blue-shifted absorption or P-Cygni profiles. In low-mass X-ray binaries (LMXBs), such signatures have been found in both the corona- and disc-dominated states. However, clear *X-ray* wind signatures have so far only been seen in the soft state (e.g. J. M. Miller et al. 2006a; G. Ponti et al. 2012, 2014; M. Díaz Trigo & L. Boirin 2016, and references therein), even though hard state outflows have been identified both in optical/near-infrared (e.g. T. Muñoz-Darias et al. 2016, 2018, 2019; F. Jiménez-Ibarra et al. 2019) and UV spectra (N. Castro Segura et al. 2022; S. Fijma et al. 2023). This raises several important questions (e.g. T. Muñoz-Darias et al. 2019; J. Sánchez-Sierras & T. Muñoz-Darias 2020; T. Muñoz-Darias & G. Ponti 2022). Is the same wind present throughout the eruption, perhaps in different ionization states? And is this wind multiphase (e.g. clumpy) and/or spatially stratified? Or are we seeing completely distinct types of outflows in different bands (e.g. cool, magnetically driven winds in the UV, optical and near-infrared bands versus hot, thermally driven winds in X-ray bands)? Resolving these issues will require panchromatic spectroscopic observations across different spectral states. In this context, this study provides the first data set allowing a search for UV wind signatures in different stages of a single outburst.

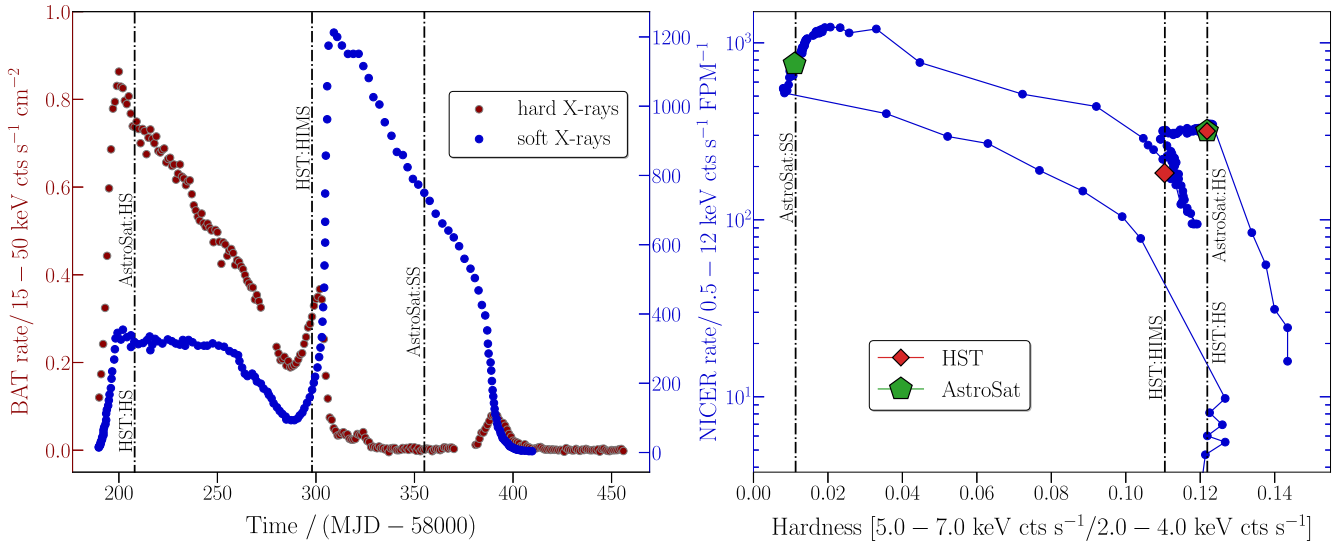

Figure 1. *Left panel*: *Swift*/BAT (hard X-rays) and *NICER* (soft X-rays) light curves of the outburst of MAXI J1820+070 in 2018. *Right panel*: *NICER* HID of the source, averaged by day. In both cases, we have superimposed the timing of our UV observations for comparison. The times of our *HST* and *AstroSat* observations are noted, signifying the respective accretion state of the system. The transition between the two X-ray states is evident in both panels.

Finally, time variability in the form of stochastic flickering and QPOs is ubiquitous among X-ray binaries (and, in fact, among all accreting systems). The standard interpretation of this variability is that each annulus of the disc is susceptible to fluctuations on its own viscous time-scale. These fluctuations then propagate inwards, so that the correlated variability we see in different wavelengths is the cumulative product of variations across a wide range of disc radii. Irradiation and reprocessing can introduce additional correlations between different wavebands on time-scales corresponding to the light travel time from the centre of the disc to the relevant emitting region. MAXI J1820+070 is already known to display correlated variability between X-rays and optical at the peak of its outburst (e.g. H. Stiele & A. K. H. Kong 2020; J. A. Paice et al. 2021; J. K. Thomas et al. 2022). Our UV data allow us to test whether/to what extent the same behaviour is present in this intermediate waveband.

MAXI J1820+070 reached peak optical brightness around March 28, but remained in the hard state until (early) July. The system then started its transition to the soft state, characterized by a rapid softening of the X-ray spectrum (J. Homan et al. 2018a, b, 2020) and a decrease of radio and infrared flux, thereby indicating quenching of the compact jet (A. J. Tetarenko et al. 2018b; P. Casella et al. 2018). In this work, we focus on three distinct snapshots of MAXI J1820+070 obtained during this outburst with the *Hubble Space Telescope* (*HST*) and *AstroSat* observatories. The timing of our observations is shown in Fig. 1, where we relate them to the overall X-ray behaviour of the system. For this purpose we have combined data from both the *Neil Gehrels Swift Observatory* (*Swift*/BAT; N. Gehrels et al. 2004; H. A. Krimm et al. 2013) and *Neutron star Interior Composition Explorer* (*NICER*; K. C. Gendreau et al. 2016) to construct both the overall X-ray light curve and the HID of the system.

2 OBSERVATIONS AND DATA REDUCTION

2.1 *Hubble Space Telescope*

MAXI J1820+070 was observed on 2018 March 31 and June 29 (Proposal ID: 15454, PI: Knigge) by the Space Telescope Imaging Spectrograph (STIS; R. A. Kimble et al. 1998; B. E. Woodgate et al. 1998) onboard *HST*. Each epoch consisted of a five-orbit *HST* visit, with three orbits dedicated to the far-UV and the remaining two to the near-UV part of the spectrum. The two visits occurred at quite different stages of the outburst evolution. The first visit took place in the *hard* state right after the outburst peak. However, the second visit took place 3 months later, during the *hard-intermediate* state (HIMS), just before the start of the hard-to-soft state transition.

The MAMA (Multi-Anode Microchannel Array) detectors were employed to obtain the observations in time-tag mode in order to provide information on the fast (dynamical time-scale) variability of the system. The initial observation, denoted as HST:HS, captured the system in a luminous hard state on MJD = 5808.5, just a few days after the outburst peak. The 0.2 arcsec × 0.2 arcsec detector slit and the *echelle* E140M/1425, E230M/1978, E230M/2707 gratings were utilized, providing us with a spectral resolution of $R = \lambda/\Delta\lambda = 45\,800$ and 30 000 in the far- and near-UV regions, respectively. The subsequent observation, designated as HST:HIMS, took place on MJD = 58298.5, just days before the state transition. In this epoch, we used the 52 arcsec × 0.2 arcsec slit coupled with the *first-order* G140L/1425 and G230L/2376 gratings. Here, the spectral resolution is not constant but wavelength-dependent on both sides of the spectrum. In particular, it ranges between 960 and 1440 in the far-UV and between 500 and 1010 in the near-UV wavelengths, respectively. A summary of the instrumental set-ups and their characteristics can be found in Table 1.

All the data were reduced using the CALSTIS pipeline to extract one-dimensional spectra for each visit. For our first epoch, blaze correction of the individual orders of the echelle spectra and trimming of their overlapping regions were applied so that we could combine them into a single spectrum. On the other hand, the construction of the HIMS first-order spectrum suffered from two challenges. First, there was a flux inconsistency between the far- and near-UV exposures – in particular, the near-UV (G230L) ods802050 exposure appeared to be 27 per cent brighter than the corresponding far-UV (G140L) one in the overlap regions between the two. We suspect that this mismatch is an instrumental artefact, possibly associated with the slight offset in the wavelength calibration discussed below (which can affect the flux level via the wavelength-dependent sensitivity

Table 1. Log of observations discussed in this work. The last column represents the notation that we are going to use throughout this paper.

Observatory	ObsID	Set-up	Onset (MJD)	Exposure (ks)	X-ray state	Notation
HST	ods801010	STIS/E140M/1425 Å	58208.52	2.151		
	ods801020	”	58208.57	2.730		
	ods801030	”	58208.64	2.730	Hard	HST:HS
	ods801040	STIS/E230M/1978 Å	58208.71	2.730		
	ods801050	STIS/E230M/2707 Å	58208.77	2.730		
HST	ods802010	STIS/G140L/1425 Å	58298.50	2.105		
	ods802020	”	58298.56	2.730		
	ods802030	”	58298.63	2.730	Hard-intermediate	HST:HIMS
	ods802040	STIS/G230L/2376 Å	58298.70	2.730		
	ods802050	”	58298.76	2.670		
AstroSat	T02_038T01_900001994	UVIT/FUV-G1	58207.50	11.39	Hard	AstroSat:HS
AstroSat	T02_066T01_900002324	UVIT/FUV-G1	58355.47	2.845	Soft	AstroSat:SS

curve). While we cannot completely rule out that this offset is real (i.e. produced by intrinsic variability), we adjusted the near-UV time-weighted average to match its far-UV counterpart. This adjustment involved determining a scaling factor based on the median value of continuum windows on both sides of the spectrum. The purpose of this choice was to facilitate our subsequent analysis by creating a single HIMS spectrum. Second, we observed a slight mismatch between the far- and near-UV line centres. As the set-up in this epoch is constrained by the lack of spectral resolution and low signal-to-noise ratio, we used the Echelle spectrum and the location of several interstellar lines as our guide to account for these wavelength shifts. In the end, we shifted the far-UV wavelengths by 1 Å and the near-UV wavelengths by 2.5 Å to correct for these offsets.

2.2 *AstroSat*

The *AstroSat* satellite observed our source on March 31 (hard state) and August 25 (soft state), utilizing its Ultraviolet Imaging Telescope (UVIT; S. Tandon et al. 2017, 2020). Here, these epochs are denoted as AstroSat:HS and AstroSat:SS, respectively.

The UVIT instrument features three channels sensitive to three different bands: far-UV (1200–1800 Å), near-UV (2000–3000 Å), and visible (3200–5500 Å). While the far- and near-UV are used for scientific observations, the visible channel primarily aids in pointing drift correction. Both the UV channels are equipped with broad-band filters for imaging, providing a point spread function (PSF) of 1.0–1.5 arcsec, and include slit-less gratings for low-resolution spectroscopy. The far-UV channel contains two orthogonally arranged slit-less gratings (FUV-G1 and FUV-G2) to minimize contamination along the dispersion direction from nearby sources. Both channels operate in the photon counting mode. Further details on grating performance and calibration can be found in G. C. Dewangan (2021).

Level-1 data on MAXI J1820+070 were sourced from the *AstroSat* archive and processed with the CCDLAB pipeline (J. E. Postma & D. Leahy 2017). Drift-corrected, dispersed images were generated orbit-wise and then aligned to produce a single image per observation. Spectral extraction was performed using the UVITTOOLS package,[1] following G. C. Dewangan (2021) and S. Kumar et al. (2023). The source's zeroth-order image position in grating images was located, and one-dimensional count spectra for the far-UV gratings in the –2 order were extracted using a 50-pixel cross-dispersion width (see S. Banerjee et al. 2024 for more details). Background count spectra were also extracted similarly from source-free regions and used to correct the source spectra. The grating responses were updated to match the simultaneous hard state *HST* spectrum of the source and these files are produced as explained in G. C. Dewangan (2021).

[1]Details about the package's requirements and documentation can be found at https://github.com/gulabd/UVITTools.jl.

3 SPECTROSCOPIC ANALYSIS

3.1 Reddening and H I column density

Most BH binaries are located at kiloparsec (kpc) distances in the Galactic plane. As a result, they tend to suffer from strong extinction and reddening, making them difficult to observe especially at UV wavelengths. In fact, only 8 out of 68 BH binary systems are characterized by reddening values $E_{B-V} \leq 0.30$ (J. M. Corral-Santana et al. 2016). In addition to MAXI J1820+070 (whose extinction properties we discuss below), these low-reddening systems are GRS 1009-45 (M. della Valle et al. 1997), XTE J1118+480 (M. Garcia et al. 2000), Swift J1357.2–0933, XTE J1817–330 (E. F. Schlafly & D. P. Finkbeiner 2011), MAXI J1305–704 (D. Mata Sánchez et al. 2021), and MAXI J0637–430 (B. E. Tetarenko et al. 2021a). Thanks to their relatively low and well-constrained extinction values, the intrinsic luminosities of these systems can be inferred with some confidence.

In order to determine the line-of-sight extinction and reddening towards MAXI J1820+070, we use two different methods. First, we fit a series of parametrized extinction curves to the UV SED. These extinction curves are characterized by the parameters A_v and R_v, where $E_{B-V} = A_v/R_v$. Here, we set $R_v = 3.1$, the standard value for Galactic sources. Using Fitzpatrick's reddening-law (E. L. Fitzpatrick 1999) to match the λ2175 interstellar dip of our 'featureless'/continuum HST:HIMS spectrum, we estimate an extinction value of $E_{B-V} = 0.20 \pm 0.05$. The quoted uncertainty here is a qualitative, but conservative estimate of the systematic uncertainty associated with this procedure. Fig. 2 illustrates how the strength of the near-UV bump changes for different extinction values. However, we will revisit how the wavelength-dependent extinction curve affects the brightness and shape of the UV SED in Section 4.2.

In addition, we exploit the well-established correlation between reddening and the neutral atomic hydrogen column density ($N_{\rm H}$) at any line of sight (e.g. R. C. Bohlin, B. D. Savage & J. F. Drake 1978; H. Liszt 2014). In our case, we determine the H I column density by modelling the damped Lyman-α (Lyα) absorption profile, evident in

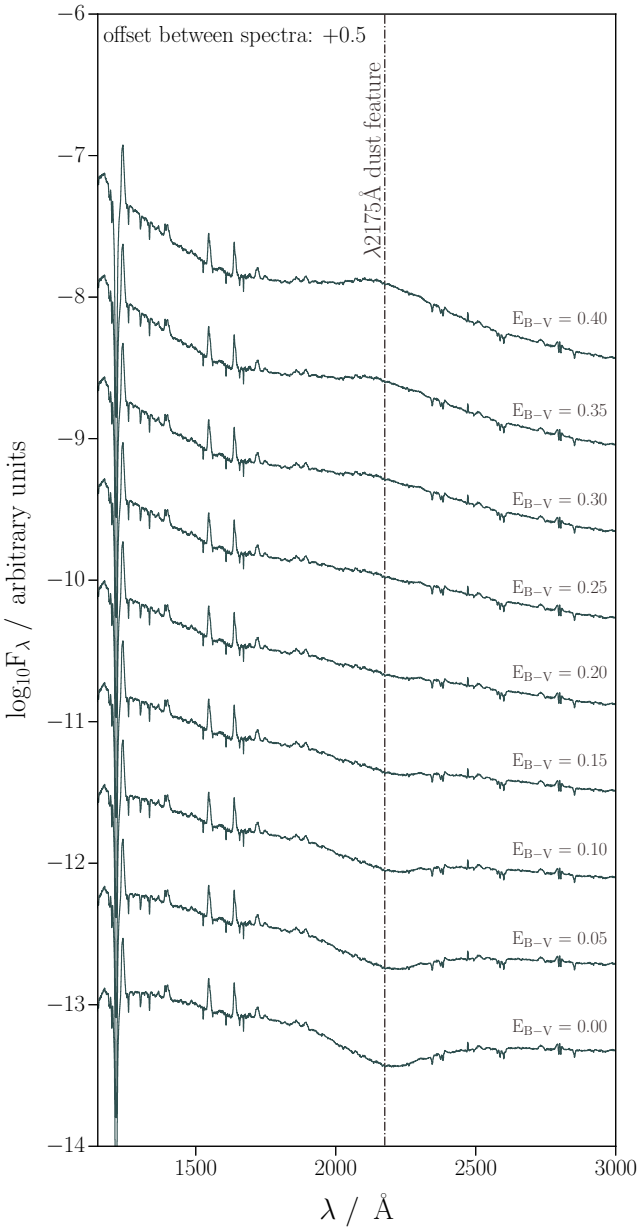

Figure 2. Modelling of the HST:HIMS spectrum to estimate the line-of-sight reddening to MAXI J1820+070. We employ the strength of the 2175 Å interstellar feature and Fitzpatrick's extinction law (E. L. Fitzpatrick 1999) to model the HST:HIMS spectrum and find the reddening value, which makes the near-UV bump to disappear. From this analysis, we derive an interstellar reddening value of $E_{B-V} = 0.20$, which is the one adopted in this paper.

our HST:HS spectrum. We follow R. C. Bohlin (1975) and model this profile by an $Ce^{-\tau}$ factor, where C is the continuum level, and the optical depth, τ, is given by

$$\tau(\lambda) = 4.26 \times 10^{-20} N_{\rm H}/(6.04 \times 10^{-10} + (\lambda - \lambda_0)^2). \quad (1)$$

Here, $\lambda_0 = 1215.67$ Å, the rest wavelength of the Lyα line. We then estimate $N_{\rm H}$ by trial and error within a range of values centred on the total line-of-sight column density. Examples of these fits are shown in Fig. 3, where the best-fitting model corresponds to a column density value of $N_{\rm H} = 10^{21}$ cm^{-2}. The corresponding reddening value then is determined via two standard $N_{\rm H}/E_{B-V}$ relations from the literature: $N_{\rm H}/E_{B-V} = 5.8 \times 10^{21}$ cm^{-2} mag^{-1} (R. C. Bohlin et al. 1978) and

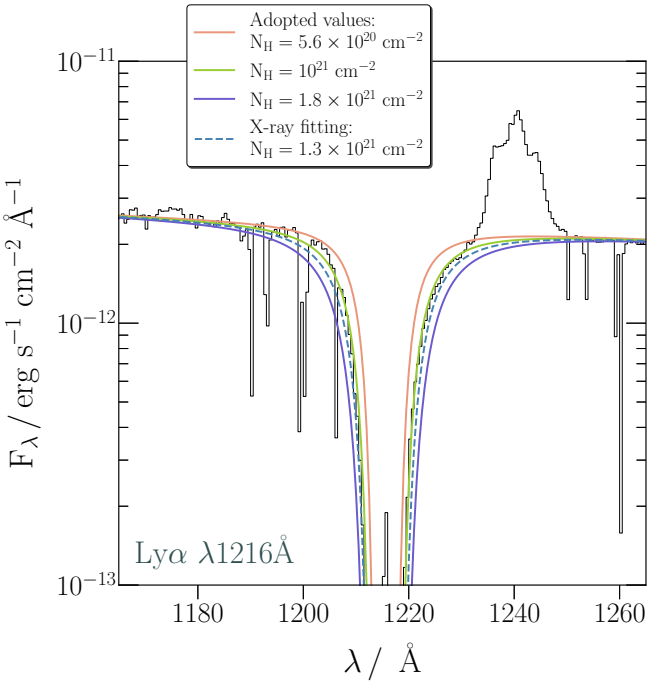

Figure 3. Modelling of the damped profile of the interstellar Lyα line in our HST:HS spectrum. The different fits are represented by different solid coloured lines, whose corresponding column density is specified in the legend. The dashed line signifies the column density, derived from X-ray spectral fitting, as described by K. I. I. Koljonen et al. (2023). The optimal model corresponds to a column density of $N_{\rm H} = 10^{21}$cm^{-2}.

$N_{\rm H}/E_{B-V} = 8.3 \times 10^{21}$ cm^{-2} mag^{-1} for $|b| < 30°$ (H. Liszt 2014). The resulting estimates for E_{B-V} towards MAXI J1820+070 are 0.17 and 0.12, respectively. These values are slightly lower, but remain consistent with the one inferred from the UV SED.

Similar reddening results are obtained when employing slightly different $N_{\rm H}$ values derived from other observational studies. For example, high-resolution 21-cm radio observations (HI4PI Collaboration 2016) and fitting of the absorbed X-ray spectrum (K. I. I. Koljonen et al. 2023) yield a column density of $N_{\rm H} = 1.3 \times 10^{21}$cm^{-2}. On the other hand, modelling of diffuse interstellar bands — such as the λ5780 line in spectra obtained with the X-Shooter instrument on the *Very Large Telescope (VLT)* — results in a column estimate of $N_{\rm H} = (1.4 \pm 0.4) \times 10^{21}$cm^{-2} (also in K. I. I. Koljonen et al. 2023). These estimates are consistent with predictions based on the Galactic dust distribution (see K. I. I. Koljonen et al. 2023 and references therein). Throughout this work, we adopt $E_{B-V} = 0.20$ as the reddening value.

3.2 Overview: spectroscopic evolution through the outburst

Our first objective is to shed light on the UV spectral evolution of MAXI J1820+070 as it passes from the hard to the soft state during its 2018 outburst. The luminous hard state near the outburst peak was covered by (quasi-)simultaneous *HST* and *AstroSat* observations. The hard-intermediate state just before the state transition was caught by our second *HST* visit, while the soft state was captured only by low-resolution *AstroSat* spectroscopy. The evolution of the source's spectrum among these three stages is shown in Fig. 4.

Overall, the *HST* spectra are characterized by blue continua and broad emission lines. Despite the significant flux decrease (by a factor of 3) and the system's transition from the hard to the soft state,

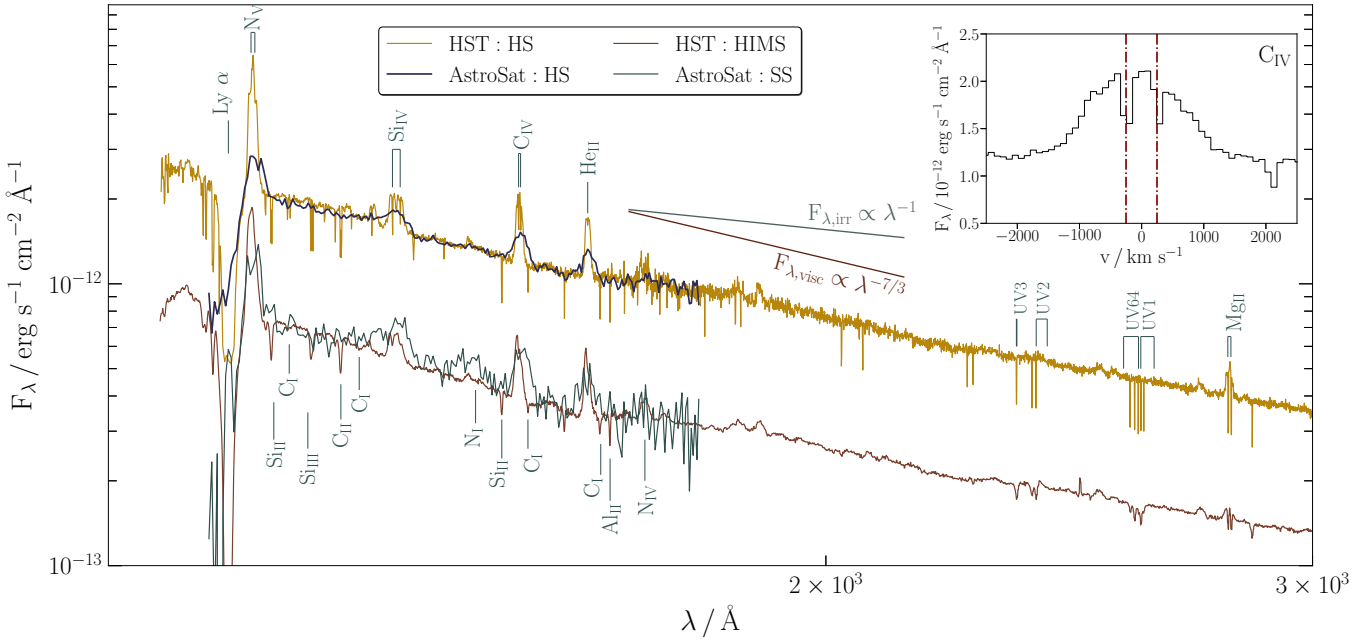

Figure 4. The dereddened time-averaged UV spectra of MAXI J1820+070 as the system evolves across three stages of its outburst, accompanied by line identifications of the most prominent species. Our work covers three distinct X-ray states of the source's outburst: (a) a luminous hard state, combining (quasi-)simultaneous *HST*/*AstroSat* observations, (b) *HST* observations of a hard-intermediate state before the state transition, and (c) *AstroSat* observations of the soft state. The *HST* spectra cover the far- and near-UV regions (1150–3000 Å) whereas the *AstroSat* observations cover only the 1200–1800 Å regime. As a reference, the slope indices of both a standard Shakura–Sunyaev accretion disc ($F_{\lambda,\mathrm{visc}} \propto \lambda^{-7/3}$) and an irradiated disc ($F_{\lambda,\mathrm{irr}} \propto \lambda^{-1}$) are illustrated. For clarity, we cut the interstellar lines by 70 per cent of their flux, compared to the original lines. The inset zooms in on the C IV λ1550 profile, emphasizing the absence of evidence for the presence of an outflow.

immediately after the second *HST* epoch, no major characteristic differences are observed between these two observations. The continuum shape remains consistent across our spectra and is reasonably well-approximated by a power law with an index close to the characteristic value for a viscously dominated accretion disc ($F_{\lambda,\mathrm{visc}} \propto \lambda^{-\beta}$, $\beta = 7/3$). This is surprising, since the disc regions producing the UV continuum may be expected to be heated by irradiation, rather than viscous dissipation. At wavelengths sufficiently far away from the Wien and Rayleigh–Jeans tails, an irradiation-dominated disc would tend to produce a power-law continuum with $\beta = 1$, significantly shallower than observed (J. Frank, A. King & D. Raine 2002). We will return to this issue in Section 4.

Both epochs display the same set of strong, double-peaked emission lines, representing both low- and high-ionization atomic transitions. At shorter wavelengths, we see strong emission features associated with UV resonance (N V λ1240, Si IV λ1400, and C IV λ1550) and recombination lines (He II λ1640). Moreover, the damped Ly α absorption line produced by absorption in the interstellar medium (ISM) contaminates the far-UV end of the spectrum. At the very opposite end, the prominent Mg II λ2800 line in emission is apparent.

The *AstroSat* spectra also capture the far-UV wavelengths, but– due to the lower resolution and signal to noise of these data sets – only the strongest lines are detected. As *AstroSat* constitutes our sole insight into the system's soft state, we exploit our simultaneous hard state observations to calibrate and facilitate comparisons between the *HST* and *AstroSat* spectra. For these comparisons, we degrade the *HST* spectra to the same resolution as the *AstroSat* observations using a simple Gaussian filter. The result is illustrated in Fig. 5. A good agreement is achieved between the (quasi-)simultaneous *HST*/*AstroSat* hard state observations, whereas there is a hint of line strengthening in the soft state, especially for the Si IV and C IV profiles.

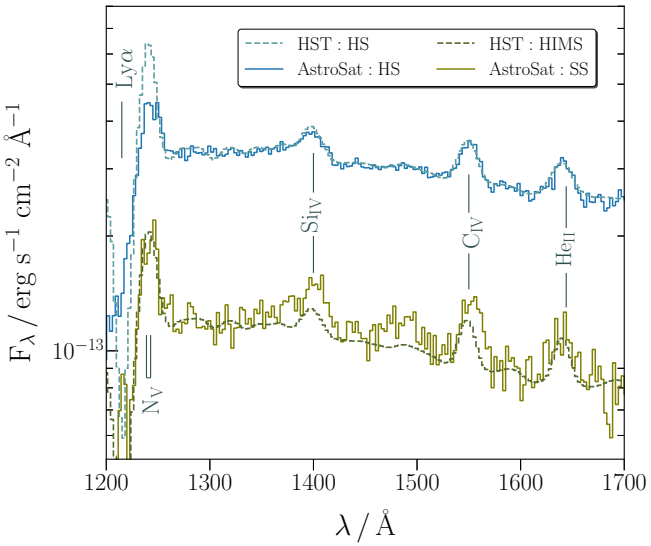

Figure 5. Far-UV spectral evolution of MAXI J1820+070 as it is captured by *HST* and *AstroSat*. We adjusted *HST*'s resolution of our hard and hard-intermediate state epochs to match *AstroSat*'s intrinsic resolution. There is apparent agreement among all the observations, taken during the hard state, whereas we observe stronger features when the system is in the soft state. We note that we have limited information regarding the line profiles in the soft state, where only four lines are visible.

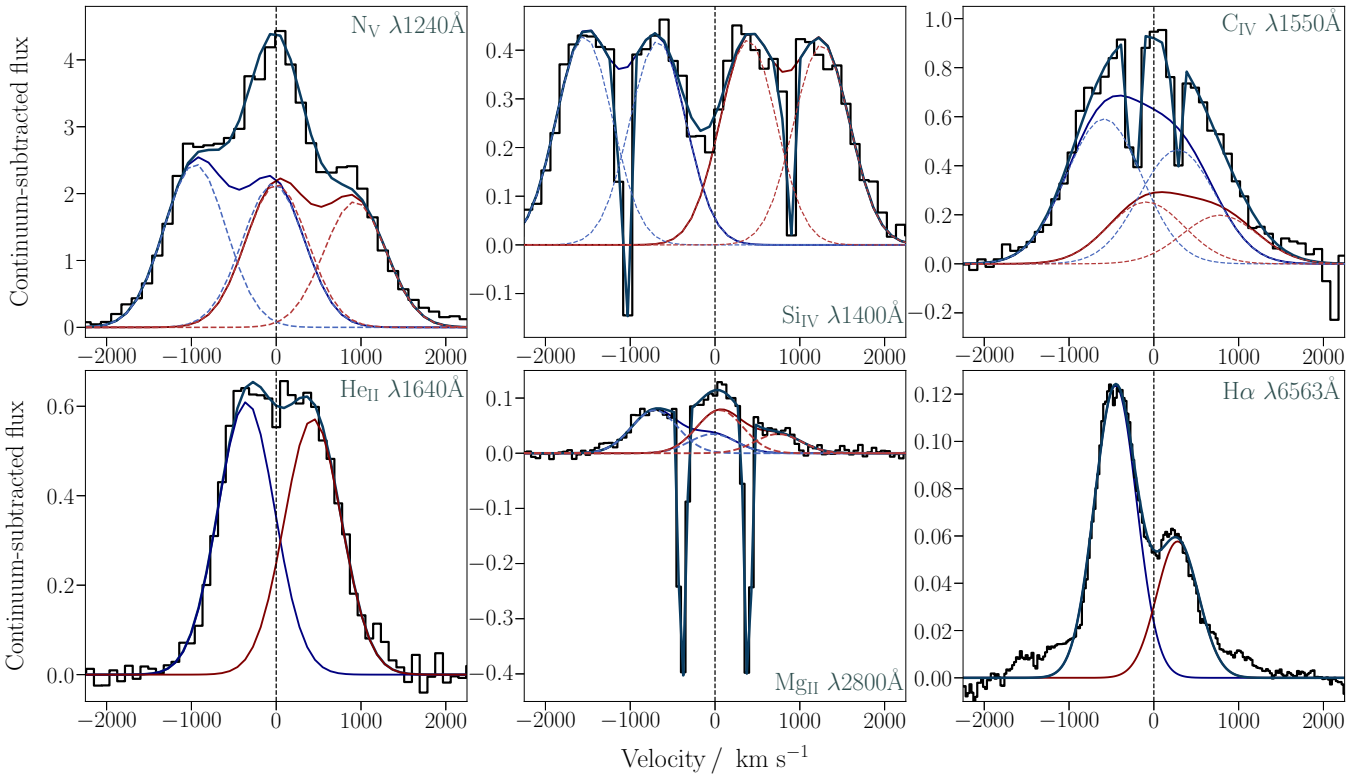

Figure 6. Continuum-subtracted line profiles of the most prominent UV resonance lines, observed during our HST:HS epoch. Each profile is fitted by a number of Gaussian components to account for each of their individual shapes (dashed lines). Our modelling is based on the fact that each atomic transition produces a distinguished blue and a red emission component. Here, we follow the blue and red colour distinction to demonstrate the relevant created profiles. The last panel shows the *VLT*/X-shooter Hα Balmer line, taken few days before the luminous hard state observation considered here, for comparison. Its profile clearly demonstrates a broad emission line wing. Details of our Gaussian modelling are provided in Table 2.

3.3 Emission line shapes and fluxes

All of the observed lines appeared to be double-peaked or consistent with being double-peaked (within the limit of the diverse spectral resolutions of our instrumental set-ups). Assuming that the observed emission lines are produced at the atmosphere of the accretion disc, their shapes can help us specify the physical conditions in the line-forming region(s) and define their evolution during the time between the observations.

Broadened, double-peaked emission profiles are characteristic of geometrically thin Keplerian accretion discs, where the two peaks correspond to regions of the disc rotating towards (blue-shifted component) or away from the observer (red-shifted component), respectively. In this context, we carry out a qualitative analysis of the most prominent observed resonance lines from our dereddened continuum-subtracted spectra. Specifically, we measure properties such as their amplitude ratios and the corresponding velocities of each of the two components. Then, the fitted emission profile is numerically integrated to extract key parameters (like their line fluxes, F_λ, and their equivalent widths, EWs).

In our fits, all relevant *atomic* transitions are assumed to produce two kinematically distinct (blue and red) Gaussian emission lines. The two components are constrained to share the same full width at half-maximum (FWHM), but they are allowed to have different normalizations and shifts relative to the relevant rest wavelengths. This is not unexpected, as transient components such as hot spots or interactions at the stream-impact bulge can disrupt the disc's model symmetry. The He II line is adequately described by two such components associated with a single atomic transition. However, most of the lines we consider (specifically N V, Si IV, C IV, and Mg II) are resonance doublets, i.e. they consist of *two* well-separated atomic transitions. We therefore have to explicitly account for both doublet components in our fits to these lines. Each of these lines is thus described by a total of four Gaussian emission profiles: an atomic doublet representing the blue kinematic component and an atomic doublet representing the red kinematic component. The wavelength separations between the atomic doublet components are always kept fixed at their known values. The intensity ratio between the doublet components is expected to range between 2:1 (in favour of the blue doublet component) and 1:1, depending on whether the line is optically thin or optically thick. However, we do not enforce this.

Our high-resolution Echelle spectra obtained in epoch HST:HS (the luminous hard state) exhibit clear evidence for narrow absorption features close to the rest wavelengths of the Si IV, C IV, and Mg II doublets. These absorption features might be intrinsic to the source, but are more likely associated with the ionized phase of the ISM along the line-of-sight. We therefore include narrow (unresolved) doublet absorption features in our models for these lines. The absorption profiles are modelled as $e^{-\tau}$, where, here, τ corresponds to the superposition of the two absorption profiles. The profiles also share the same FWHM and their intensity ratio is specified to range between 2:1 (optically thin) and 1:1 (optically thick) cases. In particular, the only line considered to be formed in an optically thick region ($\tau >> 1$) of the accretion disc is the Mg II line, as can be seen by its profile structure in Fig. 6. The same figure also shows the rest of the continuum-subtracted line profiles during our

Table 2. Attributes of the most prominent resonance line profiles in the UV region for all of our epochs. Specifically, we take a closer look at the usual suspects: the N V λ1240, Si IV λ1400, C IV λ1550, He II λ1640, and Mg II λ2800 lines. The table below summarizes various line properties, derived from Gaussian fitting of the dereddened continuum-subtracted spectra. Key properties include the integrated fluxes (in 10^{-12} erg s^{-1} cm^{-2}) and EWs along with their associated errors. Additional parameters of the fitting such as the FWHM, the individual component velocity, the peak-to-peak separation (all in km s^{-1}), the doublet amplitude ratio as well as the ratio between their red/blue component are also shown. The quoted errors correspond to 1σ (68 per cent) confidence intervals.

Line	F_λ (cgs)	$F_{\lambda,\mathrm{downgraded}}$ [a] (cgs)	EW (Å)	FWHM (km s^{-1})	σ (km s^{-1})	v_{pp} (km s^{-1})	Doublet amplitude ratio	Red-to-blue amplitude ratio
			HST:HS					
N V	32.62 ± 0.92	–	16.03 ± 0.80	1818	365	923	1.14	0.88
Si IV	6.50 ± 0.22	6.35 ± 0.33	4.00 ± 0.16	–[b]	332	867	1.02	0.98
C IV	8.71 ± 0.26	6.41 ± 0.15	7.53 ± 0.28	1773	446	869	1.27	0.43
He II	5.43 ± 0.18	5.37 ± 0.08	5.11 ± 0.19	1515	335	784	0.94	–
Mg II	1.44 ± 0.04	–	3.59 ± 0.12	1359	273	687	2.24	1.0
			HST:HIMS					
N V	13.08 ± 0.47	–	21.21 ± 1.33	2354	651	1366	3.48	1.07
Si IV	2.14 ± 0.04	–	3.98 ± 0.08	–	466	1018	1.29	0.94
C IV	2.62 ± 0.03	–	6.78 ± 0.09	2231	460	983	0.52	0.46
He II	1.92 ± 0.04	–	5.66 ± 0.14	1482	390	998	0.48	–
Mg II	0.43 ± 0.01	–	2.95 ± 0.07	1390	273	882	0.33	1.0
			AstroSat:HS					
Si IV	7.23 ± 0.72	–	4.66 ± 0.48	–	–	–	–	–
C IV	6.00 ± 0.43	–	4.98 ± 0.41	–	–	–	–	–
He II	4.84 ± 0.39	–	4.5 ± 0.39	–	–	–	–	–
			AstroSat:SS					
Si IV	3.57 ± 0.41	–	6.28 ± 0.76	–	–	–	–	–
C IV	3.59 ± 0.39	–	8.65 ± 1.01	–	–	–	–	–
He II	3.17 ± 0.74	–	9.13 ± 2.32	–	–	–	–	–
			X-shooter:HS					
Hα	0.247 ± 0.003	–	7.03 ± 0.08	649	248	732	2.14	–

[a] Line flux measurements from the downgraded dereddened continuum-subtracted spectra for an immediate comparison to the AstroSat:SS estimates. This comparison is imminently seen in Fig. 13 where we follow the line flux evolution of the source throughout the three epochs of the outburst. The respective uncertainties are estimated through Monte Carlo simulations.
[b] The big separation (≈9 Å) between the components of the Si IV λ1400 line results in doubling the apparent width and hence the FWHM of its integrated profile.

first *HST* epoch alongside the Hα Balmer profile, taken by *VLT*/X-shooter, days before our considered HST:HS date.[2] The Hα profile displays broad emission wings, reaching velocities of almost 1800 km s^{-1} (T. Muñoz-Darias et al. 2019).

In the second *HST* epoch, described by lower resolution first-order spectra, the absorption profiles are not as strikingly evident as in HST:HS and therefore, in our modelling, we fix their properties (amplitude, location, and FWHM) to their already-determined values. It is noted that, for the Mg II line, in order to facilitate the modelling process, we also fix the intensity ratio and the (common) FWHM of the four-component Gaussian emission profile to the ones of the first *HST* epoch. In all cases, the model constructed of each of the lines is smoothed to the instrumental resolution of the employed setting and then, it is rebinned to 0.5 Å.

Finally, we implement the same method to extract line properties in *AstroSat*'s dereddened spectra. However, in this case, we focus only on the strongest lines (Si IV λ1400, C IV λ1550, He II λ1640) observed in our spectra. Due to the *AstroSat*'s lower resolution, the line profiles of these species are satisfactorily fitted by two Gaussian components, except for the case of the He II line, which is well-modelled as just a single Gaussian. We avoid measuring the properties of the N V profile, as it lies too close to the blue edge of the detector to yield reliable measurements.

The line flux and EW uncertainties associated with our fits are estimated through Monte Carlo simulations. First, we estimate the standard deviation (rms), σ_{res}, between the data and the fitted model. Then, for each line, we generate mock data sets, where the model flux at each wavelength is perturbed by a Gaussian distribution centred on the actual flux with standard deviation, σ_{res}. The line flux and EW for each of these mock sets are then calculated by fitting the new line profile and numerically integrating across it. This iterative process is repeated 1000 times, allowing us to estimate the 1σ errors.

The results of our fitting process are presented in Table 2. The peak-to-peak velocities, v_{pp}, also shown in Fig. 12, are consistent with the standard picture of an accretion disc where higher ionization species are formed closer to the central source and are therefore associated with higher velocities. We will discuss the physical implications of the inferred fit parameters more in Section 6.1.1.

Our *HST* spectra show no indication of wind-formed UV features in the hard state, either in the form of blue-shifted absorption or P-Cygni profiles, as can be seen in Fig. 6. There is also no hint of such features in the *AstroSat* soft state observations, but the lower signal to noise and resolution of those observations would prevent the detection of all but the strongest such features.

[2]The *VLT*/X-shooter (J. Vernet et al. 2011) observation was acquired on 2018 March 22 (MJD = 58199.32), as part of the 0100.D-0292 programme. We processed the data using the X-shooter pipeline version 3.6.1 (W. Freudling et al. 2013).

4 IRRADIATED DISC MODELLING

X-ray irradiation is a crucial, but poorly understood, aspect of the BHXT eruptions. The reprocessing of X-ray photons can dominate over viscous heating in the outer disc, thereby generating the UV and optical light emitted in these regions (e.g. J. van Paradijs & J. E. McClintock 1994; J. van Paradijs 1996; A. R. King & H. Ritter 1998; G. Dubus et al. 2001, 1999; B. E. Tetarenko et al. 2018a). However, many aspects of this picture remain unclear, such as the dependence of the reprocessing efficiency on the irradiating SED.

As noted above (see Section 3.2 and Fig. 4), the UV continuum shape of MAXI J1820+070 seems to pose a challenge in this context. Given the high X-ray luminosity in each of our three epochs, irradiation might be expected to dominate over viscous energy release in the UV-producing disc regions. Yet the observed continuum shape is better approximated by that associated with a viscously dominated disc ($F_{\lambda,\rm visc} \propto \lambda^{-7/3}$) than that associated with an irradiation-dominated disc ($F_{\lambda,\rm irr} \propto \lambda^{-1}$). Similar behaviour has also been observed in other BHXTs, specifically Nova Muscae 1991 (F. H. Cheng et al. 1992), XTE J1859+226 (R. I. Hynes et al. 2002), and A 0620–00 (R. I. Hynes 2005). To investigate this further, we have tried to model the UV continuum more quantitatively with a model that includes both viscous and irradiation-driven heating.

Below, we first introduce our model and the irradiation contribution to the energy balance in the disc (Section 4.1). We then use the HST:HIMS spectrum as a test bed to examine whether a simple irradiated disc model can replicate the flux level and spectral shape of the observed UV SED (Section 4.2).

4.1 Description of the model

Our model describes the disc as a collection of concentric circular annuli, each of which is characterized by an effective temperature $T_{\rm eff}(R)$. The disc extends from ISCO, $R = R_{\rm ISCO}$, to an outer radius, $R = R_{\rm disc}$. The effective temperature is set by the requirement that the rate at which an annulus radiates energy away, $\sigma T_{\rm eff}^4$, must balance the rate at which energy is deposited into it by viscous dissipation and irradiation.

The viscous heating rate can be written as

$$\sigma T_{\rm visc}^4 = \frac{3GM_{\rm BH}\dot{M}_{\rm acc}}{8\pi R^3}\left[1-\left(\frac{R_{\rm ISCO}}{R}\right)^{1/2}\right], \tag{2}$$

where $M_{\rm BH}$ is the mass of the BH, and $\dot{M}_{\rm acc}$ is the accretion rate. The heating rate due to irradiation can be modelled as

$$\sigma T_{\rm irr}^4 = \left(\frac{L_{\rm irr}}{4\pi R^2}\right)\left(\frac{H}{R}\right)\gamma\,(1-A), \tag{3}$$

where $L_{\rm irr}$ is the irradiating luminosity (assumed to originate from a central point source), and A is the albedo (so that $1-A$ is the fraction of the light incident on the annulus that is absorbed). The quantity H/R is the aspect ratio of the disc, which can be shown (J. Frank et al. 2002) to scale as

$$\frac{H}{R} = \left(\frac{H}{R}\right)_{R_{\rm disc}}\left(\frac{R}{R_{\rm disc}}\right)^{\gamma}. \tag{4}$$

Here, the power-law index is usually taken to be $\gamma = 1/8$ in the absence of irradiation, and $\gamma = 2/7$ if irradiation dominates the heating rate (c.f. J. Frank et al. 2002). Strictly speaking, γ is therefore a function of radius, but we neglect this here and simply set $\gamma = 2/7$ everywhere. This approximation means that we will slightly overestimate the influence of irradiation, but only in disc regions where irradiation is relatively unimportant anyway.

Putting all of this together, the effective temperature of the disc can be calculated by requiring that total heating should be matched by radiative cooling, i.e.

$$\sigma T_{\rm eff}^4 = \sigma T_{\rm visc}^4 + \sigma T_{\rm irr}^4. \tag{5}$$

In order to calculate the spectrum of the disc, we assume that each annulus radiates as a modified blackbody,

$$B_{\nu,\rm mod}(f, T_{\rm eff}) = \frac{2h\nu^3}{f^4c^2\left[e^{\frac{h\nu}{fkT_{\rm eff}}}-1\right]}. \tag{6}$$

Here, f is the so-called spectral hardening factor (T. Shimura & F. Takahara 1995), which approximately corrects for the effects of Compton scattering in the disc atmosphere. This factor is not actually a constant, but rather is a function of temperature, surface density and radius (and, for BHs, spin parameter). In our SED model, we parametrize f using the analytical fitting function provided by S. W. Davis & S. El-Abd (2019). In calculating the required surface density, we take into account the relevant relativistic correction factors (I. D. Novikov & K. S. Thorne 1973; S. W. Davis & S. El-Abd 2019). In our specific application of the model to UV observations here, the effects of spectral hardening are negligible.

4.2 Disc SED modelling

Our primary focus is to assess if irradiation significantly impacts the outer accretion disc regions and can reproduce the shape and flux level of the far- and near-UV SED. To achieve this, we opt to model the spectrum prior to the state transition (HST:HIMS) as it provides us a unique opportunity for a direct comparison of our model, which is close in time and luminosity, with the one employed by K. I. I. Koljonen et al. (2023), henceforth referred to as the 'reference model'. We note that in our performed modelling, we fix $L_{\rm x} = 1.35 \times 10^{38}$erg s^{-1} (K. I. I. Koljonen et al. 2023).

We first try to find the optimal model that describes our dereddened UV SED. We allow the mass accretion rate ($\dot{M}_{\rm acc}$), outer disc radius ($R_{\rm out}$), and albedo ($A_{\rm out}$) to vary, taking into account both irradiation heating and viscous dissipation. It is important to mention that we cannot avoid the mathematical degeneracy between albedo and scale height, so we opt to fix the latter for simplicity. We assume a Schwarzschild (non-spinning) BH (J. Guan et al. 2021; X. Zhao et al. 2021), scale height $H/R = 0.10$ while the orbital characteristics (d, $M_{\rm BH}$, i, q) of the system are already determined (P. Atri et al. 2020; M. A. P. Torres et al. 2020). In particular, we adopt $M_{\rm BH} = 8.5\,{\rm M}_\odot$ and i $= 65^\circ$ in our modelling, while all the distances are measured with respect to the gravitational radius, $R_{\rm G} = GM_{\rm BH}/c^2$.

The best-fitting model SED is shown in Fig. 7 (upper panel). As already noted above, the observed spectral shape of the UV continuum is close to that of a standard accretion disc without any irradiation. In line with this, the UV emitting regions in our best-fitting model are *viscously dominated*, with very little, contribution from irradiation. However, the parameters of our optimal model – $\dot{M}_{\rm acc} = 10^{-7}$ M$_\odot$ yr^{-1} $\simeq 0.5\dot{M}_{\rm Edd}$, $R_{\rm out} = 10^6 R_{\rm G}$, $A_{\rm out} = 0.93$ – are physically implausible. In particular, the radius of the outer disc is much greater than the radius of the *tidal disc* of the BH accretor, as $R_{\rm out} \approx 4 \times R_{\rm tidal}$. For reference, the tidal radius is estimated as $R_{\rm tidal} = 10^{5.4} R_{\rm G}$.

Can a physically more plausible irradiated disc model still reproduce the SED acceptably? Naively, for any reasonable values of the disc parameters ($\dot{M}_{\rm acc}, R_{\rm out}, A_{\rm out}$), irradiation should play a crucial role. To address this question more directly, we construct a small grid of models that allows us to understand how changes in these

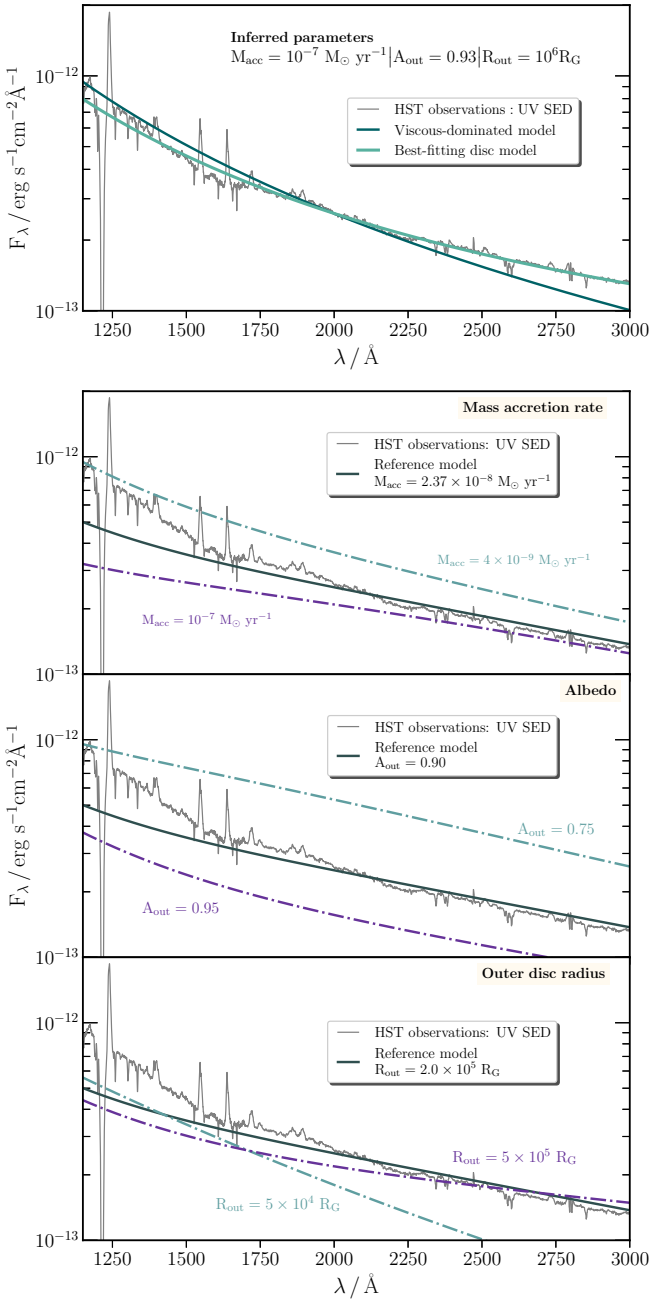

Figure 7. Modelling of the UV SED of MAXI J1820+070 during the epoch preceding the hard-to-soft state transition (HST:HIMS). *Upper panel*: The best-fitting model for our SED is very close to a pure viscous-dominated disc. This model results in a set of unrealistic values for parameters such as $M_{acc}, A_{out}, R_{out}$, making it unsuitable for describing the system. *Lower panel*: Parameter sensitivity analysis in our modelling to evaluate the dependency and impact of the considered disc factors on the final output. Each panel corresponds to one of these factors, where we explore a plausible range of their parameter space (dash–dotted lines), overlaid on the observed HST:HIMS UV spectrum (grey colour) of MAXI J1820+070. The reference disc UV SED, as modelled by K. I. I. Koljonen et al. (2023), is included in dark grey across all panels for context.

parameters affect the overall SED (and the irradiation contribution, specifically). Our grid is roughly centered on the 'reference' disc SED model of K. I. I. Koljonen et al. (2023). This model is derived by fitting the X-ray-optical SED of MAXI J1820+070 at the soft state, days after the hard/soft state transition. The corresponding reference parameters are $\dot{M}_{acc} = 2.37 \times 10^{-8}$ $M_\odot$ yr^{-1}, $R_{out} = 10^{5.3} R_G$, and $A_{out} = 0.9$. The attempted comparison is justified, as the two epochs are close enough in time that we do not expect the values of the considered parameters to change significantly.

Fig. 7 (lower triplet of panels) shows the reference and test models that make up our small grid overlaid on the UV SED of the hard-intermediate state. The reference model is clearly too red and underestimates the far-UV flux level. Moreover, even though our test models confirm that reasonable changes to the model parameters can certainly modify the UV continuum, they also suggest that such changes cannot simultaneously match the brightness and shape of the observed SED. Could extinction effects resolve this discrepancy? To test this, we examined two parametrizations of the Fitzpatrick's extinction law: one varying the R_V parameter (E. L. Fitzpatrick 1999) and another probing the far-UV non-linear rise (through the c4 parameter; E. L. Fitzpatrick & D. Massa 1990). Neither R_V (across a reasonable range) nor c4 (within physically plausible values) could reconcile the SED with the reference model. We will discuss the implications of this result in Section 6.3.

5 TIMING ANALYSIS

In this section, we search for and analyse the variability in our UV data set. This is particularly interesting because the emission produced in the *outer* accretion disc is likely to peak in this waveband. To this end, we first construct wavelength-integrated light curves from our time-resolved observations, and then the corresponding PDS, where the variability amplitude (power) is expressed as a function of frequency.

The light curves are generated using the LIGHTCURVE package.[3] They are both background-subtracted and corrected for buffer dumps. An overview of the light curves for all epochs can be seen in Fig. 8. Rapid, aperiodic variability is apparent throughout the observations. More specifically, the far-UV light curves obtained during the HST:HS observations clearly exhibit flaring activity with a fractional rms amplitude of $\simeq 10$ per cent. The corresponding flaring amplitude in the near-UV is $\simeq 7$ per cent.

Rather suspiciously, all of the light curves obtained from the HST:HIMS visit in Fig. 8 exhibit a slow rise in count rate at the beginning of each orbit. Following discussions with the STScI office and a detailed inspection of the cross-dispersion profiles during this visit, we tentatively attribute these variations to instrumental focus changes. We therefore opt to filter out these slow variations by fitting a second-order polynomial to the respective light curves and then normalizing them to this fit. The polynomial fits are shown overlaid on the raw HST:HIMS light curves in Fig. 8. We then measure the fractional rms amplitudes of the short-term variability in each orbit, which is $\simeq 4$ per cent and $\simeq 3$ per cent in the far- and near-UV, respectively.

Next, we construct the PDS following the methodology by S. Vaughan (2005). We define the periodogram for a light curve with K points and ΔT sampling rate as the modulus-squared of the discrete Fourier transform (DFT), $X(f_j)$,

$$I(f_j) = \frac{2\Delta T}{< x >^2 N} |X_j|^2, \tag{7}$$

evaluated at the Fourier frequencies $f_j = j/K\Delta T$ with $j = 1,2,\ldots,$ $K/2$. Its normalization is in (rms/mean)^{2}Hz^{-1}, expressing the power

[3]The original code is available at https://github.com/justincely/lightcurve, but we have adapted the code to suit our requirements.

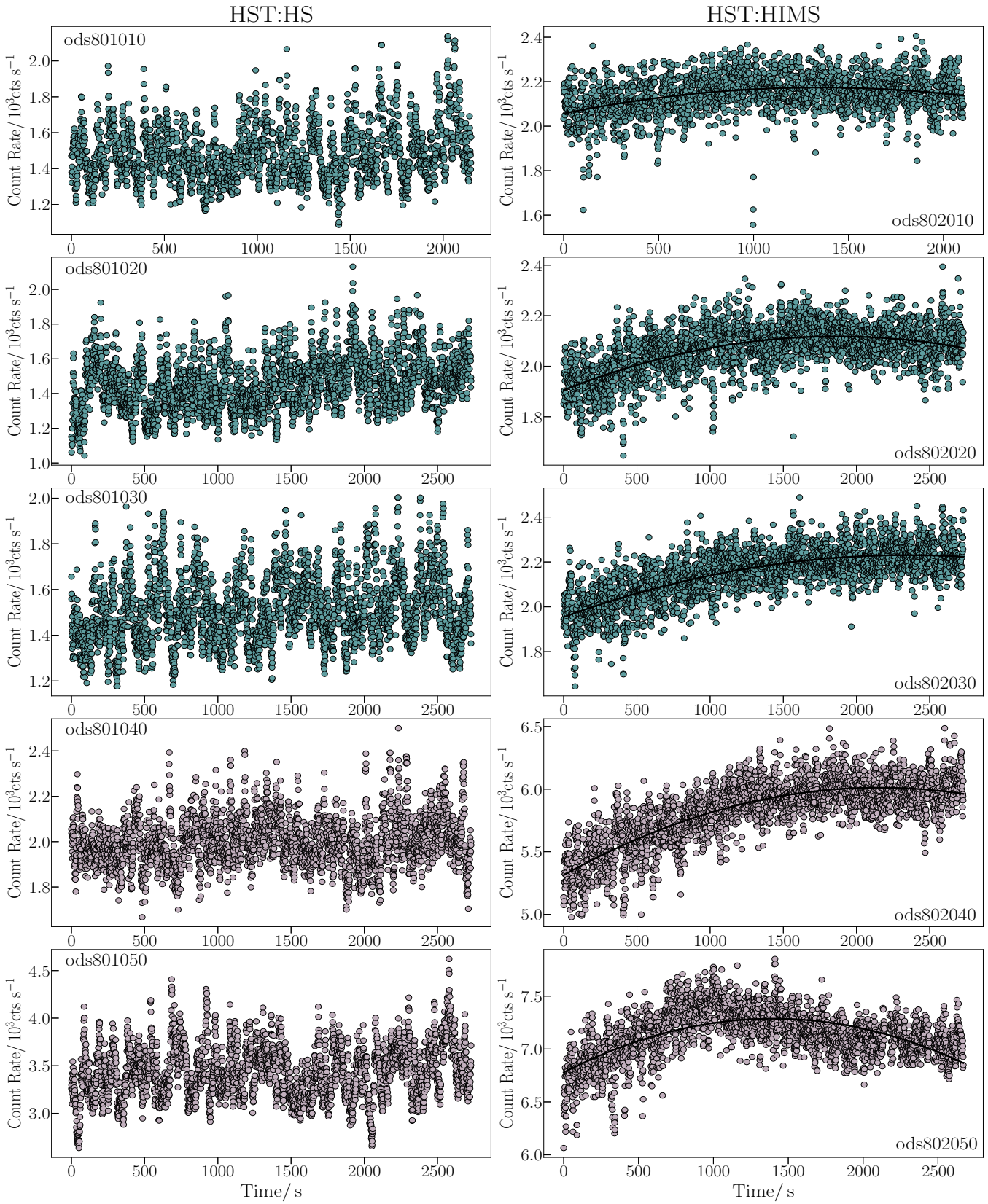

Figure 8. Far- and near-UV light curves of MAXI J1820+070, extracted at one-second resolution, for both the hard state and hard-intermediate state observations, taken by *HST*. As noted, the left column showcases light curves of the first luminous hard state (HST:HS) while the right column features the corresponding light curves of the hard-intermediate state (HST:HIMS). For our HST:HIMS observations, we overlaid our polynomial fit, correcting for the presented turnover. The two colours are utilized to distinguish between the far- (teal) and near-UV observations (dusty pink). For completion, we have also noted the obsID of the considered observations at each of the panels.

in fractional units (M. van der Klis 1989, 1997; S. Vaughan et al. 2003; S. Vaughan 2005).

One of our aims here is to examine our data sets for the presence of any significant sharp features, e.g. low-frequency quasi-periodic oscillations (LF-QPOs), as seen in X-ray and optical studies (e.g. S. P. Mudambi et al. 2020; H. Stiele & A. K. H. Kong 2020; J. A. Paice et al. 2021; D.-M. Mao et al. 2022; J. K. Thomas et al. 2022). Overall, our UV PDS exhibit a pattern consistent with that seen in other sources and at other wavelengths. The 'continuum', i.e. broad-band noise, can be aptly described by a single-bend power law with two distinct power indices, delineated by the break frequency. At the highest frequencies, the power spectra are governed by Poisson noise. Finally, especially during our HST:HS observations, we do observe a weak yet discernible signature of a QPO close to the break frequency, within the frequency range dominated by red noise, and at a frequency that is similar to QPOs detected in other bands.

We decided to take a closer look at the power spectra in which we tentatively detect a peak. Specifically, we use the method outlined by S. Vaughan (2005) to determine the statistical significance of these detections. This involves first fitting each observed PDS with two models, one with and one without a QPO component. In these fits, the intrinsic red-noise 'continuum' is described as a broken (or bending) power law, while the QPO is approximated as a Lorentzian of a centroid frequency, υ_c, and FWHM width, W_q. A likelihood ratio test is then used to assess whether the model including the QPO fits the data significantly better. Both the centroid frequency and the width of the QPO are treated as free parameters in the fits including this component. The method also automatically accounts for the number of trials (i.e. the number of frequencies for which the power spectrum is calculated).

The full PDS model that includes the QPO is given by D. P. Summons et al. (2007)

$$P(\nu) = \frac{A_{\rm BPL}\nu^{\alpha_{\rm L}}}{1+(\frac{\nu}{\nu_{\rm B}})^{\alpha_{\rm L}-\alpha_{\rm H}}} + \frac{B_{\rm QPO}Q\nu_{\rm c}}{\nu_{\rm c}^2+4Q^2(\nu_{\rm c}-\nu)^2} + C_{\rm PS}. \quad (8)$$

Here, the first term describes the broken power law (BPL) continuum with $\nu_{\rm B}$ the break frequency, and $\alpha_{\rm L}$, $\alpha_{\rm H}$, the low- and high-frequency indices. The second term accounts for the presence of the QPO with the parameter Q, known as the quality factor (measure of coherence), aptly connected to the centroid frequency as υ_c/W_q. The third term, $C_{\rm PS}$, describes the variability associated with Poisson noise. The parameters $A_{\rm BPL}$ and $B_{\rm QPO}$ serve as normalization constants for the individual components. In the model without a QPO, the second term is simply set to zero.

Following S. Vaughan (2005), we use the maximum likelihood estimation (MLE) method and the S-statistic to determine the optimal fit parameters. All model parameters are allowed to vary. We then assess the goodness of fit in both cases using the Kolmogorov–Smirnov (KS) test, comparing the data/model residual ratio with the theoretical χ^2 distribution of two degrees of freedom, χ^2_2, for unbinned periodograms. Further details[4] can be found in S. Vaughan (2005) and references therein. The uncertainties in our best-fitting parameters are estimated by Monte Carlo simulations. For each data set, we generate 1000 mock exponentially distributed PDS and fit them in the same manner as described earlier. This iterative process provides us with the best-fitting parameters and S-statistic for each mock data set, allowing us to estimate 1σ errors from the 16 per cent and 84 per cent quantiles. The best-fitting parameters and their uncertainties, as well as details of our fitting results, are summarized in Table 3.

Fig. 9 presents the different PDS for both the far- and near-UV regions, where we have also superimposed both the QPO and non-QPO models. In Fig. 10, we additionally illustrate the contributions of the different components. In both cases, we indicate the estimated centroid frequencies in both the X-ray (H. Stiele & A. K. H. Kong 2020; D.-M. Mao et al. 2022) and optical (D.-M. Mao et al. 2022) wavelengths, with respect to the time of our UV observations. Taken separately, both models provide statistically acceptable fits to the data.

In order to test if the QPOs are significantly detected, we once again follow S. Vaughan (2005) in estimating their statistical significance. Specifically, we use the likelihood ratio test (LRT) to check if the additional freedom associated with the QPO model is warranted by the data. The test statistic here is

$$\Delta S = S_1 - S_2 = -2\ln[\mathcal{L}_1/\mathcal{L}_2], \quad (9)$$

where indices 1 and 2 represent the likelihoods and S-statistics for the simpler and complex models, respectively. If the models are nested, and the simpler model is correct, the variable ΔS is χ^2_ν−distributed, where ν is the number of additional free parameters. In our case, ΔS therefore follows a χ^2_3 distribution under the null hypothesis that the no-QPO model is correct (since the QPO term requires three additional parameters). The p-values associated with this null hypothesis turn out to be 0.044, 0.014, 0.044 for the far-UV and 0.0067, 0.069 for the near-UV range. These values correspond to 2σ–3σ detections of the QPOs – suggestive, but not definitive. A stacking analysis – i.e. splitting each light curve into segments and stacking the resulting PDS – might help to confirm or reject this, but implementing this is beyond the scope of this paper. For now, given that the locations of the putative UV QPOs are consistent with those seen in other bands, we tend to think that they are likely real and worthy of consideration.

We also constructed a PDS from both the raw and corrected light curves of our HST:HIMS observations. Notably, all the raw PDS exhibit an unusual excess at low frequencies, in line with our suspicion that the slow variations in these data sets are instrumental artefacts. This low-frequency excess disappears once the polynomial fit is used to 'correct' the light curves. An illustrative example of this process is presented in Fig. 11. There are no hints of QPO feature in HST:HIMS, in any of the visits associated with this epoch. Given this, and also the inevitable uncertainty associated with our polynomial correction, we choose not to perform detailed PDS modelling for this epoch.

6 DISCUSSION

6.1 The spectral evolution through the accretion states

6.1.1 Probing the accretion states

Accretion states in BHXTs are usually defined in terms of their X-ray properties. Do their UV properties reflect the same phenomenological picture?

MAXI J1820+070 provide us with a rare opportunity to investigate, for the first time in the UV band, the long-term spectral evolution of a BH binary as it transitioned from the hard to the soft state. Interestingly, we find that the UV behaviour remains surprisingly consistent across both states: there are no distinct signatures that would signal the state transition or the different

[4]We compare the data/model residual ratio to a theoretical χ^2_2 distribution as the real and imaginary terms of a DFT are normally distributed and their superposition follows a χ^2_2 variable.

Table 3. Best-fitting model parameters of the considered models for the HST:HS PDS both at the far- and near-UV range.

ObsID	$\log A^a_{\rm BPL}$	$\alpha^b_{\rm L}$	$\alpha^c_{\rm H}$	$\nu^d_{\rm B}$ (mHz)	$\log B^e_{\rm QPO}$	$\log Q^f$	$\nu^g_{\rm c}$ (mHz)	$C^h_{\rm PS}$	KS-Test ^{i}	ΔS^j
					HS: far-UV @1425 Å					
ods801010	-0.044 ± 0.53	0.042 ± 0.23	-2.52 ± 0.19	20.93 ± 5.42	-3.10 ± 0.25	1.01 ± 0.49	52.79 ± 1.63	$(2.38 \pm 0.21) \times 10^{-3}$	0.74	
	-0.9 ± 0.35	-0.31 ± 0.16	-3.09 ± 0.26	38.60 ± 7.53	–	–	–	$(2.63 \pm 0.19) \times 10^{-3}$	0.62	0.044
ods801020	-1.20 ± 0.40	-0.44 ± 0.18	-2.95 ± 0.35	37.44 ± 11.25	-3.07 ± 0.30	0.77 ± 0.47	55.34 ± 2.48	$(2.67 \pm 0.19)\,10^{-3}$	0.97	
	-1.30 ± 0.25	-0.475 ± 0.13	-3.47 ± 0.27	49.85 ± 7.24	–	–	–	$(2.81 \pm 0.15) \times 10^{-3}$	0.86	0.014
ods801030	-0.057 ± 0.58	0.024 ± 0.24	-2.95 ± 0.98	16.00 ± 4.55	-2.75 ± 0.24	0.18 ± 0.19	54.65 ± 5.82	$(2.84 \pm 0.14)\,10^{-3}$	0.46	
	-1.63 ± 0.28	-0.62 ± 0.14	-3.56 ± 0.32	49.31 ± 8.48	–	–	–	$(2.96 \pm 0.13) \times 10^{-3}$	0.61	0.044
					HS: near-UV @1978 Å					
ods801040	-1.22 ± 0.38	-0.20 ± 0.18	-3.63 ± 0.55	28.88 ± 5.11	-3.80 ± 0.28	0.82 ± 0.40	57.81 ± 2.11	$(2.26 \pm 0.083) \times 10^{-3}$	0.48	
	-1.48 ± 0.29	-0.30 ± 0.14	-3.88 ± 0.41	37.40 ± 5.10	–	–	–	$(2.25 \pm 0.080) \times 10^{-3}$	0.39	0.0067
					HS: near-UV @2707 Å					
ods801050	-0.075 ± 0.055	0.054 ± 0.22	-2.49 ± 0.15	14.65 ± 3.29	-3.97 ± 0.96	1.44 ± 3.00	56.13 ± 0.90	$(1.28 \pm 0.087) \times 10^{-3}$	0.74	
	-0.85 ± 0.45	-0.256 ± 0.19	-2.70 ± 0.17	21.64 ± 4.69	–	–	–	$(1.33 \pm 0.082) \times 10^{-3}$	0.83	0.069

Note. All the uncertainties are 1σ (68 per cent) confidence intervals. The second line of each observation corresponds to our modelling without the Lorentzian contribution. [a] BPL normalization constant. [b] Low-frequency (before the break) power-law index. [c] High-frequency power-law index. [d] Break frequency. [e] Normalization constant of the Lorentzian, describing the QPO. [f] Quality factor defined as $\nu_{\rm c}/W_{\rm q}$, where W_q the FWHM of the Lorentzian. [g] Centroid frequency of the QPO peak. [h] Poisson constant. [i] Goodness-of-fit p-value obtained via the KS-test. [j] Statistical significance of the QPO obtained through the LRT test.

phases of the hard-state decay. This phenomenon may come as a surprise if we consider the case of the BHXT XTE J1859+226 (R. I. Hynes et al. 2002), where we do observe evolution of the spectrum during different stages of its outburst decay. The UV spectra exhibit the same Doppler-broadened, double-peaked line profiles, which are most likely emitted by an optically thin layer of the disc's atmosphere.

Given the velocities determined from our modelling of the line profiles, we can estimate the location of the corresponding line-forming regions by assuming that the peak-to-peak separation of a given line corresponds to the Keplerian velocity near (the outer edge of) the disc region in which the line is produced. This line formation radius estimate is therefore given by

$$R = \pm \frac{\mathrm{GM_{BH}} \sin^2 i}{v^2_{\rm pp}} \Rightarrow R = \frac{c^2 \sin^2 i}{v^2_{\rm pp}} [R_{\rm G}], \tag{10}$$

where the latter equation is expressed in terms of $R_{\rm G}$. This quantity is shown for each line in each *HST* epoch in Fig. 12, where we also relate this to the ionization potential of the relevant species. As expected, the higher ionization lines are generated at smaller radii, where the temperatures are higher, while the lower ionization lines originate in the cooler parts of the disc further out.

Fig. 13 compares the fluxes of the key lines (i.e. N V λ1240, Si IV λ1400, C IV λ1550 or He II λ1640, Mg II λ2800) between our three independent epochs: the luminous hard state (HST:HS), the hard-intermediate state just before the state transition (HST:HIMS) and the soft state (AstroSat:SS). Two key features are apparent. First, the line fluxes decline by approximately a factor of 3 between the hard state and the hard-intermediate state observations. This is similar to the drop in the UV continuum flux between these epochs, i.e. the EWs of the lines remain almost unchanged. Second, line fluxes then increase again – by roughly a factor of 2 – between HST:HIMS and the soft state.

The strengthening of the UV lines across the hard-to-soft state transition may be expected, given the increase in EUV and soft X-ray luminosity across this transition (Fig. 1). The line strength evolution between the hard state and hard-intermediate state observations seems less obvious. Although the soft X-ray luminosity in HST:HIMS *is* lower than that in HST:HS (Fig. 1), the difference amounts to less than a factor of 2. Moreover, one might expect the strong hard X-ray component in HST:HS to *inhibit* the formation of the UV lines, by overionizing the material in the disc atmosphere.

However, it is important to remember that the radial locations of the line-forming regions are not the same in HST:HS and HST:HIMS. Fig. 12 shows that all of the characteristic line-formation radii move *inward* – by slightly less than a factor of 2 – between HST:HS and HST:HIMS. This is consistent with each line being formed preferentially at a characteristic ionization parameter, $\mathrm{U} \propto L/\mathrm{n_e}R^2$. If the density in the line-forming layers of the disc atmosphere is roughly constant, we expect the characteristic line-forming radius for a given line to scale with luminosity as $R \propto L^{1/2}$. The evolution we see in line flux and velocity evolution between HST:HS and HST:HIMS is therefore likely due to the combination of these factors.

6.1.2 *Absence of evidence for UV winds*

The classic observational wind signatures are blue-shifted absorption or P-Cygni line profiles, although these features are strongly inclination-dependent (e.g. G. Ponti et al. 2012; M. Díaz Trigo et al.

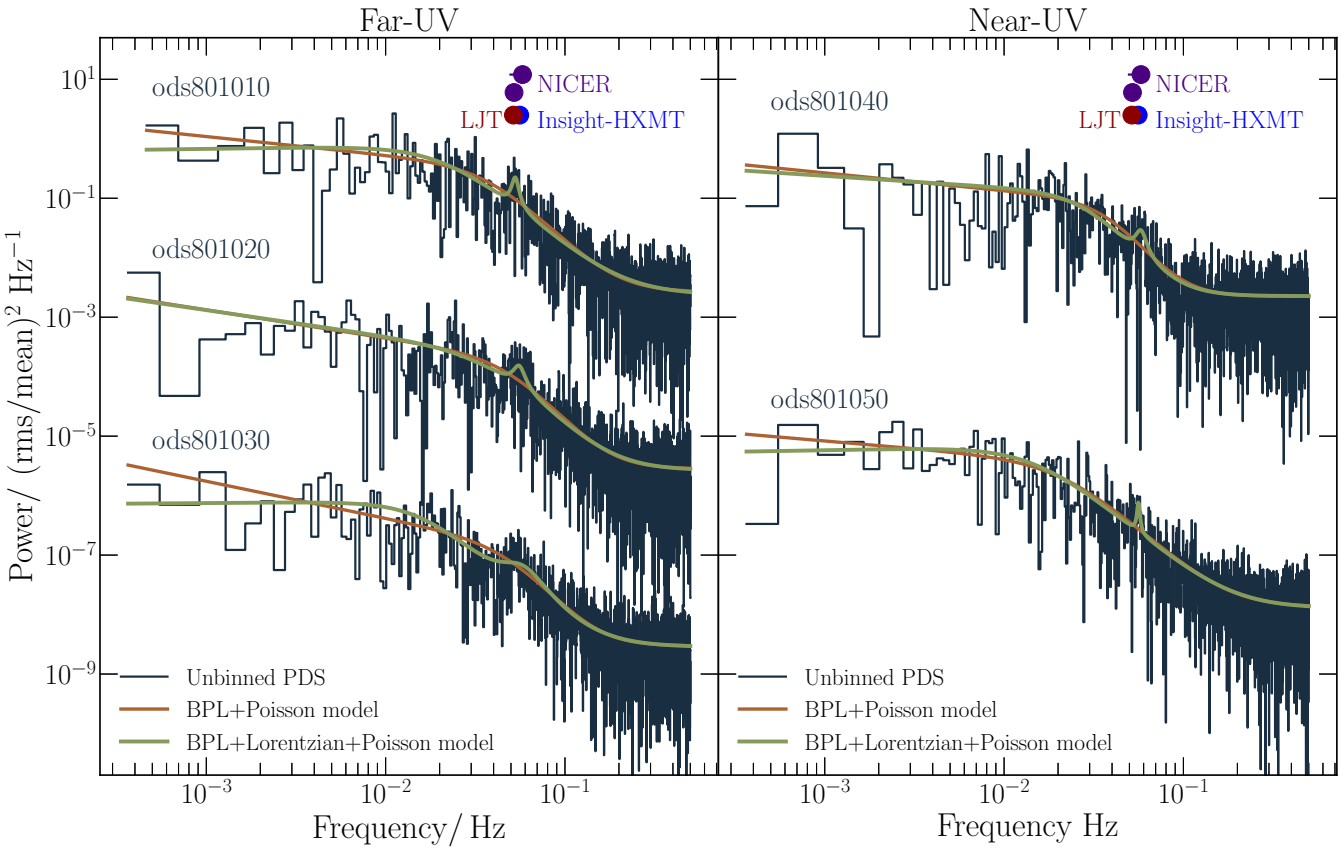

Figure 9. The PDS for both the far- (left) and near-UV (right) wavelengths during our HST:HS epoch are presented. The different solid lines represent the best-fitting models, incorporating the Lorentzian contribution. Tentative evidence for the presence of a LF-QPO is observed in the far-UV, which is absent in the near-UV observations. For reference, characteristic centroid QPO frequencies, estimated in the X-ray (NICER; H. Stiele & A. K. H. Kong 2020, Insight-HMXT/HE; D.-M. Mao et al. 2022) and optical (LJT/YFOSC; W. Yu et al. 2018; D.-M. Mao et al. 2022) bands, close to our observation time, are displayed.

2014; M. Díaz Trigo & L. Boirin 2016). The response of these signatures to X-ray luminosity variations and state transitions is of great interest, but difficult to explore.

In this study, only our hard state *HST* observation has the signal to noise and resolution to allow a sensitive search for UV wind signatures in MAXI J1820+070. However, we find no evidence for these in the usual UV resonance lines (see Fig. 6 for more information).

The absence of outflow signatures prompts the question: is the wind truly absent or are we merely unable to detect it? Notably, winds in the hard state have been detected both in optical (T. Muñoz-Darias et al. 2019) and near-infrared (J. Sánchez-Sierras & T. Muñoz-Darias 2020) spectra of this source. These detections mainly manifested as P-Cygni and blue emission line wing features in Balmer/Helium and Paschen lines, respectively.

Among known LMXBs, clear UV wind signatures have so far only been seen in Swift J1858.6–0814 (N. Castro Segura et al. 2022) and UW CrB (S. Fijma et al. 2023). However, there are very few systems with UV observations in which such signatures could have been found. Moreover, the signatures in Swift J1858.6–0814 are weak and transient, making them quite difficult to detect. The absence of evidence for a 'warm' outflow can therefore not yet be interpreted as evidence for its absence. More UV data – for multiple systems and across different accretion states – will be needed to address this issue.

6.2 The evolutionary history of the binary

The relative strengths of the UV resonance lines can serve as sensitive indicators of the physical conditions in the line-emitting gas. However, they can also be used as a complementary tool to determine the evolution of a system by estimating the initial mass of the donor and its evolutionary history. More specifically, the abundance and/or depletion of elements, such as N v and C iv, have been linked to the life stage and status of the companion. The key physics here is that the CNO cycle becomes the dominant nuclear process in stars with an initial mass of $M_2 \geq 1.4\,M_\odot$ (D. D. Clayton 1983). Hence the abundance N v/C iv ratio emerges as a reliable signature to discern whether the gas stream of the accreting material has undergone CNO-processing (e.g. C. W. Mauche et al. 1997; C. A. Haswell et al. 2002; B. T. Gänsicke et al. 2003; C. S. Froning et al. 2011, 2014; N. Castro Segura et al. 2024).

The relevant line ratios of MAXI J1820+070 are plotted in Fig. 14 along with the corresponding ratios for other systems, ranging from CVs to LMXBs. It appears that our source displays line ratios that are characteristic of 'normal' CVs, suggesting that the accreting material has *not* undergone CNO processing. For reference, Fig. 14 also includes comparison systems with anomalous line ratios. In these systems, the donor star is usually thought to have had an initial mass $\gtrsim 2M_\odot$. Its envelope was then stripped during a thermal time-scale mass-transfer phase, leading to present-day surface abundances that

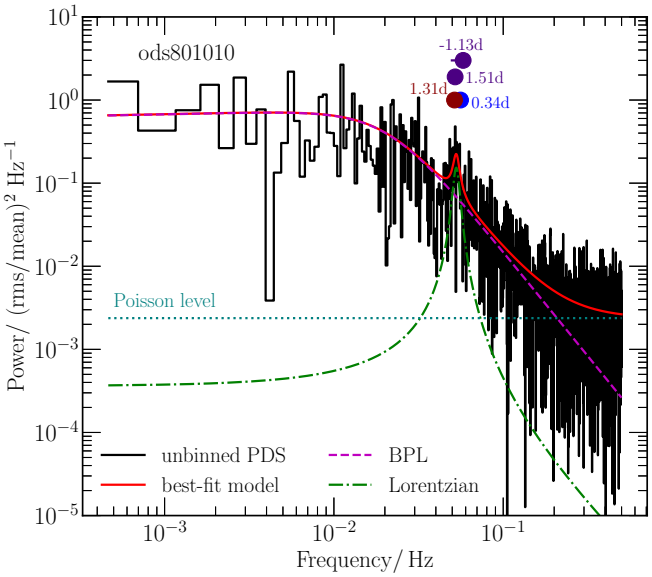

Figure 10. Example of a far-UV PDS of our source during our HST:HS observations, showing a weak signature of a QPO. The solid line represents the overall best-fitting model while the dashed and dash–dotted lines highlight the two main model contributions (BPL: dashed, Lorentzian: dash-dotted). The level of Poisson noise is seen as a dotted line. The X-ray and optical QPO frequencies, mentioned in Fig. 9, offer valuable context for comparison.

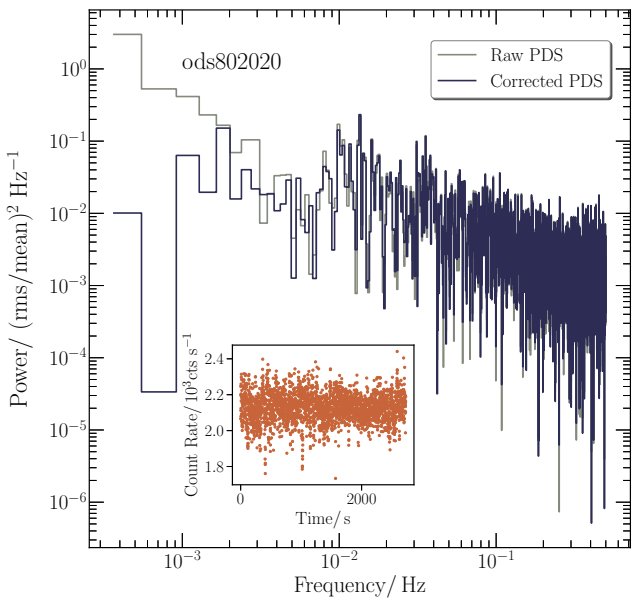

Figure 11. Representative far-UV PDS of the HST:HIMS epoch of MAXI J1820+070. We overlaid both the raw and corrected PDS to illustrate the difference prior and after the applied correction. The corresponding corrected light curve is placed as an inset.

reflect the earlier phase of CNO processing in the core (K. Schenker et al. 2002).

Given the well-determined distance ($d = 2.96 \pm 0.33$ kpc) of MAXI J1820+070 (P. Atri et al. 2020) and its low reddening value, there have already been efforts to determine its binary parameters. These suggest a BH primary with mass $M_{\rm BH} = (5.95 \pm 0.22)\sin^{-3} i\, {\rm M}_\odot$ and a K-type (sub-giant) companion (M. A. P. Torres et al. 2020; J. Mikołajewska et al. 2022). Our results here imply that this donor is not the descendant of an initially much more massive star.

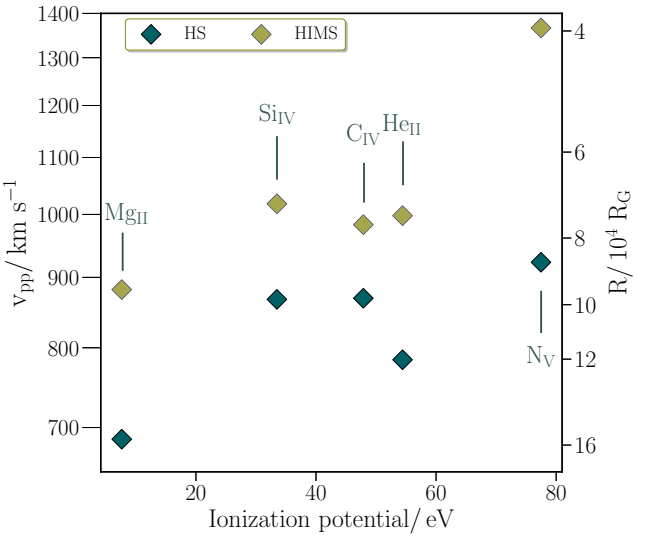

Figure 12. The peak-to-peak velocities, $v_{\rm pp}$, of the main atomic species for our *HST* hard state and hard-intermediate state, as a function of their ionization potential. On a secondary axis, we depict the corresponding radii (in $R_{\rm G}$ units) where these species are formed in the disc. High-ionization emission lines are formed closer to the central object whereas low-ionization species are situated further out at the outer disc. For both epochs, the line-forming regions are located within the tidal radius.

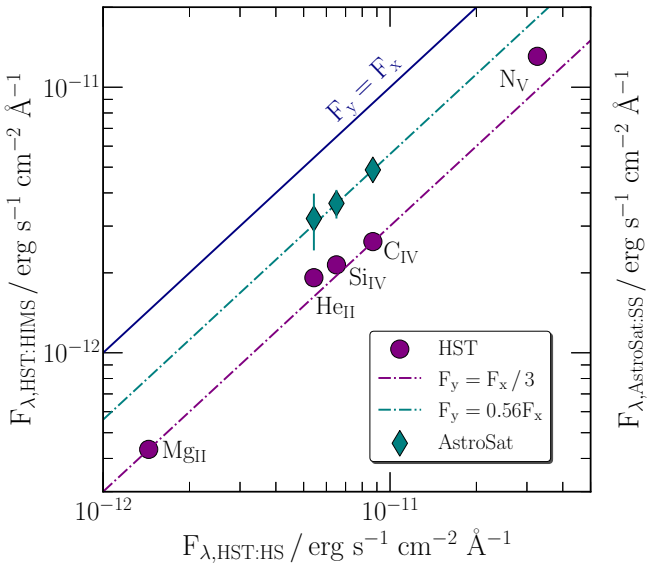

Figure 13. The plot compares the line fluxes of MAXI J1820+070 across our considered epochs. We use the HST:HS fluxes as our reference point along the *x*-axis and compare them with their HST:HIMS and AstroSat:SS counterparts. For a fair comparison between the *HST* and *AstroSat* fluxes (as different settings are employed), we applied a correction to the AstroSat:SS fluxes. The correction includes the introduction of a factor, $f_{\rm corr}$, which is defined as the ratio of the line fluxes obtained from HST:HS to their adjusted counterparts. The straight lines indicate specific scalings, purely as a visual guide.

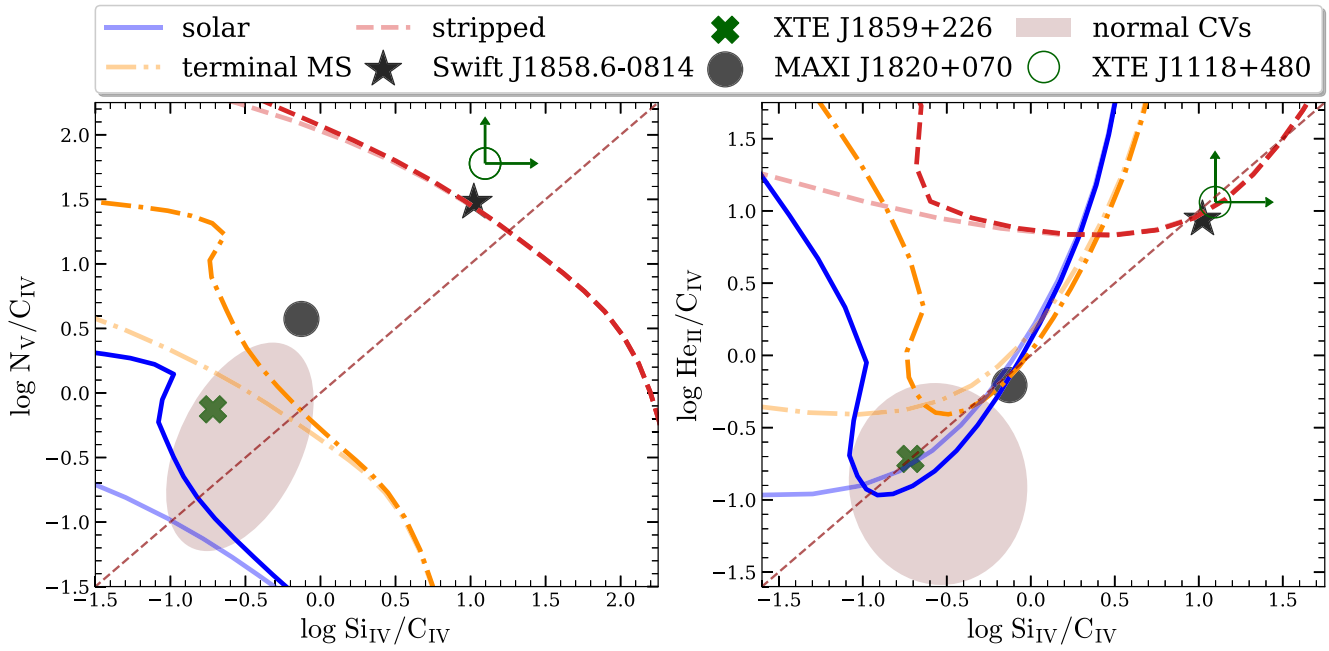

Figure 14. Far-UV emission-line flux ratios for LMXBs: XTE J1118+480, XTE J1859+226 (C. A. Haswell et al. 2002), Swift J1858.6–0814 (N. Castro Segura et al. 2024). The region of the parameter space occupied by the 'normal' CVs presented in C. W. Mauche et al. (1997) and B. T. Gänsicke et al. (2003) is indicated with the shaded region, which encloses 2.5σ of a two-dimensional (2D) Gaussian distribution. The lines are predicted line ratios as a function of the ionization parameter computed with CLOUDY for an optically thin parcel of gas irradiated with a simple accretion disc presented above in Section 4.1. Solid, dash–dotted and dashed lines are models carried out with solar abundances, $M \approx 1.5 - 2.0\,\mathrm{M}_{\odot}$ terminal main sequence (MS) and the equilibrium CNO-cycle core of a $M \approx 2.0\,\mathrm{M}_{\odot}$ star, respectively. The latter is labelled as stripped, as we consider to have representative abundances of a stripped star with its convective CNO core exposed. The models include the O IV multiplet within range of the Si IV doublet. For reference, lines including the emission only from Si IV are shown with the same linestyle but higher transparency. The measurements of MAXI J1820+070 (filled black circle) at different epochs overlay in the plot but for clarity, a single measurement is shown. MAXI J1820+070 lies very close to the theoretical predictions for a terminal MS star.

6.3 Is irradiation important?

As shown in Section 4, the UV continuum shape, shown in Fig. 7, cannot be adequately described by a simple irradiated disc model with physically plausible parameters. This is mainly because the spectral shape is close to that of a viscously dominated, unirradiated disc, similar to what happens in Nova Muscae 1991 (F. H. Cheng et al. 1992) and A 0620–00 (R. I. Hynes 2005). For physically reasonable parameters, the model is a poor match to the data, especially at the shortest far-UV wavelengths. Yet, X-ray irradiation is certainly *expected* to heat up the outer parts of the disc.

A related puzzle is that one might expect reprocessing to be quite sensitive to both the luminosity and SED of the X-ray radiation field. Yet the observed UV spectra are actually fairly similar across all three spectral states. The UV continuum luminosity tracks the drop in X-ray luminosity between the hard and hard-intermediate states, but then actually stays constant across the hard-to-soft state transition. The emission line strengths also track the declining X-ray luminosity between the hard and hard-intermediate states, before partially recovering in the soft state. However, the headline result is that both the continuum spectral shape and the dominant emission lines remain virtually unchanged, even as the system moves through three very different accretion states.

We can gain some insight into the implications of these observational findings by examining the physics underlying our simple irradiated disc model. In this model, X-rays are produced by point-like, isotropically emitting source at the centre of the disc. Some of these X-ray photons impact on the disc surface and are absorbed there. This heats up the irradiated parts of the disc, thus increasing the effective temperature and modifying the radial intensity profile.

In reality, the details of this process are complex (e.g. G. Dubus et al. 1999). The geometry and location of the X-ray emitting 'corona' are highly uncertain, but clearly important. Similarly, the shape and scale height of the disc – $H/R|_R$ – are key factors in determining what fraction of X-ray photons are intercepted by the disc. However, the relevant scale height here is *not* really the pressure scale height, but rather the height above the disc at which it presents an optical depth of $\simeq 1$ *to the irradiating photons*. Finally, the detailed physics governing the reprocessing of X-rays in the disc atmosphere are clearly far more complex than what can be captured by a single efficiency parameter (i.e. the albedo).

It is easy to see that some or all of these processes are expected to depend on the accretion state of the source. For example, the opacity the disc atmosphere presents to incoming X-ray photons, as well as the efficiency with which those photons are reprocessed, are sensitive to whether these photons are soft or hard. And yet the presumably reprocessing-dominated UV emission-line spectrum remains qualitatively unchanged.

Part of the explanation may be that the relevant parts of the disc do not see the same X-ray SED that we do, and that the formation of UV emission lines is mainly controlled by EUV photons. For reference, by 'EUV', here we mean photons with energy between, say, 13.6 and 100 eV (check Fig. 12, which includes the ionization potentials of the relevant species). In fact, the He II recombination line is generally thought to be a reliable bolometer for the EUV luminosity above 54 eV (or, in this case, the fraction of this luminosity that is intercepted by the disc).

As noted above, the He II emission line flux drops by $\simeq \times 3$ between the luminous hard state (HST:HS) and hard-intermediate state (HST:HIMS) before partially recovering in the soft state (AstroSat:SS). On the one hand, these relatively modest variations are in line with the modest changes in the observed emission line spectra. And indeed, the soft X-ray flux also only varies by a comparable amount (see Fig. 1).

On the other hand, the He II line flux is clearly not proportional to the soft X-ray flux: the latter is comparable in the hard and hard-intermediate states, but a factor of $\simeq \times 3$ higher in the soft state. Moreover, the *hard* X-ray component completely dominates in HST:HS, is comparable to the soft X-ray component in HST:HIMS, and is all but completely quenched in AstroSat:SS. So, somehow, the UV line-forming regions must be shielded from the ionizing effects of the energetic X-ray photons produced in the hard state.

Our main conclusion from all these considerations is that the physics governing the reprocessing of X-rays in the outer disc regions is (a) complex and (b) poorly described by simple models. We therefore strongly encourage theoretical efforts to construct physically realistic models of irradiated accretion disc atmospheres.

6.4 Evidence of a UV QPO signal?

Only a handful of systems to date are known to display LF-QPOs in multiple wave bands (mostly in the optical/infrared and in X-rays; check C. Motch, S. A. Ilovaisky & C. Chevalier 1982; C. Motch et al. 1983; R. I. Hynes et al. 2003; M. Durant et al. 2009; P. Gandhi et al. 2010, for more information). The only system known to exhibit an analogous signal in the UV is the BHXT XTE J1118+480 (R. I. Hynes et al. 2003). The mentioned studies are based on panchromatic, (quasi-)simultaneous observations of BHXTs and correspond to periods when the systems are in the low hard state. It is still unclear, though, whether the X-ray and longer wavelength signals are physically associated and how the latter are actually produced (e.g. S. Markoff et al. 2001; R. I. Hynes et al. 2003; A. Veledina, J. Poutanen & I. Vurm 2013; A. Veledina & J. Poutanen 2015; P. Gandhi et al. 2017).

In this work, our time-resolved observations allow us to search for UV QPO signatures only in the *hard* state. Nevertheless, MAXI J1820+070 is already known to display simultaneous X-ray and optical LF-QPOs in the hard state, as reported by D.-M. Mao et al. (2022) and J. K. Thomas et al. (2022). In this state, the observed X-ray QPOs, the so-called type-C QPOs, may be associated with a precessing hot flow near the inner edge of the disc (e.g. L. Stella & M. Vietri 1998; A. Ingram et al. 2009; A. R. Ingram & S. E. Motta 2019), instabilities in the disc (e.g. M. Tagger & R. Pellat 1999; P. Varnière et al. 2002, 2012) or corona variability (e.g. L. Titarchuk & R. Fiorito 2004; C. Cabanac et al. 2010). On the other hand, in the optical band, detections of QPOs are limited, and the observed signals are usually attributed to precession (A. Veledina et al. 2013), thermal reprocessing (A. Veledina & J. Poutanen 2015) or jet synchrotron emission variations (e.g. S. Markoff et al. 2001; R. I. Hynes et al. 2003; P. Gandhi et al. 2017).

Almost at the time of our observations, D.-M. Mao et al. (2022) and J. K. Thomas et al. (2022) find that both X-ray and optical signals share similar centroid QPO frequencies and evolve similarly over time. However, optical variations are more coherent, i.e. $Q_{\rm X-ray} < Q_{\rm opt}$ (check table 1 in D.-M. Mao et al. 2022). This implies that disc reprocessing is not the dominant mechanism, and X. Ma et al. (2021) suggest instead that the jet may precess at the QPO frequency.

Our work provides provisional evidence for the existence of UV LF-QPOs with centroid frequencies closely resembling those observed in other bands. Our modelling suggests – albeit taking into account only the observations when we *do* detect a QPO – that the coherence in the UV is lower than the equivalent one in optical and X-rays (for almost the same centroid frequencies). It seems unlikely that synchrotron radiation could be responsible for QPOs in the UV band. The current results suggest that the 'same' type-C QPOs in different bands can be produced in three distinct regions–the inner accretion flow (producing X-ray QPOs), the jet (producing optical QPOs) and the outer disc (producing UV QPOs via reprocessing). In the UV, reprocessing may constitute the primary mechanism, which is in line with the lower coherence we observe.

7 SUMMARY

We have presented the first multi-epoch, time-resolved, and spectrally resolved UV characterization of the transient X-ray binary MAXI J1820+070. We obtained observations in three distinct stages of the outburst: a luminous hard state after the eruption peak, a hard-intermediate state just before the state transition and finally the soft state.

Our main conclusions are the following:

(i) We have determined the interstellar reddening and extinction towards the source via the λ2175 absorption feature (near-UV bump) and Lyα modelling. Our estimate of the reddening is quoted as $E_{B-V} = 0.20 \pm 0.05$.

(ii) We track the spectral evolution of MAXI J1820+070 throughout its outburst. Surprisingly, we see no major differences in the appearance of the UV emission line spectrum across the three distinct spectral states. The UV spectra are characterized by blue continua with superposed broad, double-peaked emission lines, such as N V λ1240, Si IV λ1400, C IV λ1550, He II λ1640, Mg II λ2800.

(iii) We do not find evidence of an outflow in the form of blue-shifted absorption or P-Cygni profiles in any of the considered lines that are mentioned above.

(iv) We use the relative strengths of the UV resonance lines to constrain the evolutionary history of the binary, showing that the donor had not undergone CNO processing in the past and presumably now lies at the end of the MS or at the sub-giant branch.

(v) Simple irradiated disc models with physically plausible parameters fail to adequately describe the observed UV continuum shape. This is mainly because the observed spectral slope is close to that for an unirradiated, viscously dominated accretion disc.

(vi) There is marginal evidence for a UV LF-QPO signature in the data obtained during the luminous hard state (HST:HS). The frequencies of these candidate QPOs are comparable to those of QPOs detected almost at the same time in X-ray and optical observations of MAXI J1820+070. This provisional evidence is worthy of consideration and if confirmed, these signatures may be produced through reprocessing at the outer disc regions.

ACKNOWLEDGEMENTS

We sincerely appreciate our referee for their valuable feedback, which improved the quality of this manuscript. We also thank Dr. Douglas Buisson for providing us with the *NICER* data products and Dr. Andrés Gúrpide Lasheras for helpful discussions. MG acknowledges support by the Mayflower scholarship in the School of Physics and Astronomy of the University of Southampton. NCS acknowledge support from the Science and Technology Facilities Council (STFC) grant ST/X001121/1. Partial support for KSL's effort on the project was provided by NASA through grant numbers HST-GO-16489 and

HST-GO-16659 from the Space Telescope Science Institute, which is operated by AURA, Inc., under NASA contract NAS 5-26555. RIH acknowledges support from NASA through the grant number HST-GO-15454 from the Space Telescope Science Institute, which is operated by AURA, Inc., under NASA contract NAS 5-26555.

This work was conducted with the help of NUMPY (S. van der Walt, S. C. Colbert & G. Varoquaux 2011), ASTROPY (Astropy Collaboration 2018), SCIPY (P. Virtanen et al. 2020), and MATPLOTLIB (J. D. Hunter 2007).

DATA AVAILABILITY

The main data sets underlying this study are publicly available through their respective archives:

HST/MAST archive – https://archive.stsci.edu/.

AstroSat/ISSDC archive – https://astrobrowse.issdc.gov.in/astro_archive/archive/Home.jsp.

Complimentary data sets in X-rays (*Swift*) and optical (*VLT*) are found on the HEASARC (https://swift.gsfc.nasa.gov) and ESO webpages (http://archive.eso.org), respectively. The *NICER* data products were provided to us following private communication with the author.

REFERENCES

Astropy Collaboration, 2018, AJ, 156, 123
Atri P. et al., 2020, MNRAS, 493, L81
Baglio M. C., Russell D. M., Lewis F., 2018, Astron. Telegram, 11418, 1
Banerjee S. et al., 2024, ApJ, 964, 189
Belloni T. M., 2010, in Belloni T., ed., Lecture Notes in Physics, Vol. 794, The Jet Paradigm: From Microquasars to Quasars. Springer, Berlin, p. 53
Belloni T. M., Motta S. E., 2016, in Bambi C., ed., Astrophysics and Space Science Library, Vol. 440, Astrophysics of Black Holes: From Fundamental Aspects to Latest Developments. Springer, Berlin, p. 61
Belloni T. M., Stella L., 2014, Space Sci. Rev., 183, 43
Belloni T., Homan J., Casella P., van der Klis M., Nespoli E., Lewin W. H. G., Miller J. M., Méndez M., 2005, A&A, 440, 207
Bohlin R. C., 1975, ApJ, 200, 402
Bohlin R. C., Savage B. D., Drake J. F., 1978, ApJ, 224, 132
Cabanac C., Henri G., Petrucci P. O., Malzac J., Ferreira J., Belloni T. M., 2010, MNRAS, 404, 738
Casella P., Belloni T., Homan J., Stella L., 2004, A&A, 426, 587
Casella P., Testa V., Russell D. M., Belloni T. M., Maccarone T. J., 2018, Astron. Telegram, 11833, 1
Castro Segura N. et al., 2022, Nature, 603, 52
Castro Segura N. et al., 2024, MNRAS, 527, 2508
Cheng F. H., Horne K., Panagia N., Shrader C. R., Gilmozzi R., Paresce F., Lund N., 1992, ApJ, 397, 664
Clayton D. D., 1983, Principles of Stellar Evolution and Nucleosynthesis. Univ. Chicago Press, Chicago
Corbel S. et al., 2001, ApJ, 554, 43
Corbel S., Nowak M. A., Fender R. P., Tzioumis A. K., Markoff S., 2003, A&A, 400, 1007
Corral-Santana J. M., Casares J., Muñoz-Darias T., Bauer F. E., Martínez-Pais I. G., Russell D. M., 2016, A&A, 587, A61
Davis S. W., El-Abd S., 2019, ApJ, 874, 23
della Valle M., Benetti S., Cappellaro E., Wheeler C., 1997, A&A, 318, 179
Dewangan G. C., 2021, J. Astrophys. Astron., 42, 49
Díaz Trigo M., Boirin L., 2016, Astron. Nachr., 337, 368
Díaz Trigo M., Migliari S., Miller-Jones J. C. A., Guainazzi M., 2014, A&A, 571, A76
Done C., Gierliński M., Kubota A., 2007, A&AR, 15, 1
Dubus G., Lasota J.-P., Hameury J.-M., Charles P., 1999, MNRAS, 303, 139
Dubus G., Hameury J. M., Lasota J. P., 2001, A&A, 373, 251
Durant M., Gandhi P., Shahbaz T., Peralta H. H., Dhillon V. S., 2009, MNRAS, 392, 309
Esin A. A., McClintock J. E., Narayan R., 1997, ApJ, 489, 865
Fender R., Gallo E., 2014, Space Sci. Rev., 183, 323
Fender R. et al., 1999, ApJ, 519, L165
Fender R. P., Belloni T. M., Gallo E., 2004, MNRAS, 355, 1105
Fender R. P., Homan J., Belloni T. M., 2009, MNRAS, 396, 1370
Ferreira J. et al., 2022, A&A, 660, A66
Fijma S., Castro Segura N., Degenaar N., Knigge C., Higginbottom N., Hernández Santisteban J. V., Maccarone T. J., 2023, MNRAS, 526, L149
Fitzpatrick E. L., 1999, PASP, 111, 63
Fitzpatrick E. L., Massa D., 1990, ApJS, 72, 163
Frank J., King A., Raine D., 2002, Accretion Power in Astrophysics, 3rd edn. Cambridge Univ. Press, New York, p. 398
Freudling W., Romaniello M., Bramich D. M., Ballester P., Forchi V., García-Dabló C. E., Moehler S., Neeser M. J., 2013, A&A, 559, A96
Froning C. S. et al., 2011, ApJ, 743, 26
Froning C. S., Maccarone T. J., France K., Winter L., Robinson E. L., Hynes R. I., Lewis F., 2014, ApJ, 780, 48
Gandhi P. et al., 2010, MNRAS, 407, 2166
Gandhi P. et al., 2017, Nat. Astron., 1, 859
Gänsicke B. T. et al., 2003, ApJ, 594, 443
Garcia M., Brown W., Pahre M., McClintock J., Callanan P., Garnavich P., 2000, IAU Circular, 7392, 2
Gehrels N. et al., 2004, ApJ, 611, 1005
Gendreau K. C. et al., 2016, in den Herder J.-W. A., Takahashi T., Bautz M., eds, Proc. SPIE Conf. Ser. Vol. 9905, Space Telescopes and Instrumentation 2016: Ultraviolet to Gamma Ray., SPIE, Bellingham, p. 420
Gilfanov M., 2010, in Belloni T., ed., Lecture Notes in Physics, Vol. 794, The Jet Paradigm: From Microquasars to Quasars. Springer, Berlin, p. 17
Grove J. E., Johnson W. N., Kroeger R. A., McNaron-Brown K., Skibo J. G., Phlips B. F., 1998, ApJ, 500, 899
Guan J. et al., 2021, MNRAS, 504, 2168
Hameury J. M., 2020, Adv. Space Res., 66, 1004
Haswell C. A., Hynes R. I., King A. R., Schenker K., 2002, MNRAS, 332, 928
HI4PI Collaboration, 2016, A&A, 594, A116
Higginbottom N., Knigge C., Long K. S., Matthews J. H., Sim S. A., Hewitt H. A., 2018, MNRAS, 479, 3651
Higginbottom N., Knigge C., Long K. S., Matthews J. H., Parkinson E. J., 2019, MNRAS, 484, 4635
Higginbottom N., Knigge C., Sim S. A., Long K. S., Matthews J. H., Hewitt H. A., Parkinson E. J., Mangham S. W., 2020, MNRAS, 492, 5271
Homan J., Belloni T., 2005, Astrophys. Space Sci., 300, 107
Homan J., Wijnands R., van der Klis M., Belloni T., van Paradijs J., Klein-Wolt M., Fender R., Méndez M., 2001, ApJS, 132, 377
Homan J. et al., 2018a, Astron. Telegram, 11820, 1
Homan J. et al., 2018b, Astron. Telegram, 11823, 1
Homan J. et al., 2020, ApJ, 891, L29
Hunter J. D., 2007, Comput. Sci. Eng., 9, 90
Hynes R. I., 2005, ApJ, 623, 1026
Hynes R. I., Haswell C. A., Chaty S., Shrader C. R., Cui W., 2002, MNRAS, 331, 169
Hynes R. I. et al., 2003, MNRAS, 345, 292
Ingram A. R., Motta S. E., 2019, New Astron. Rev., 85, 101524
Ingram A., Done C., Fragile P. C., 2009, MNRAS, 397, L101
Jiménez-Ibarra F., Muñoz-Darias T., Casares J., Armas Padilla M., Corral-Santana J. M., 2019, MNRAS, 489, 3420
Kawamuro T. et al., 2018, Astron. Telegram, 11399, 1
Kimble R. A. et al., 1998, ApJ, 492, L83
King A. R., Ritter H., 1998, MNRAS, 293, L42
Koljonen K. I. I., Long K. S., Matthews J. H., Knigge C., 2023, MNRAS, 521, 4190
Krimm H. A. et al., 2013, ApJS, 209, 14
Kumar S., Dewangan G. C., Singh K. P., Gandhi P., Papadakis I. E., Tripathi P., Mallick L., 2023, ApJ, 950, 90
Lasota J., 2001, New Astron. Rev., 45, 449
Liszt H., 2014, ApJ, 780, 10

Ma X. et al., 2021, Nat. Astron., 5, 94
Mao D.-M., Yu W.-F., Zhang J.-J., Yan Z., Rapisarda S., Wang X.-F., Bai J.-M., 2022, Res. Astron. Astrophys., 22, 045009
Markoff S., Falcke H., Fender R., 2001, A&A, 372, L25
Mata Sánchez D., Rau A., Álvarez Hernández A., van Grunsven T. F. J., Torres M. A. P., Jonker P. G., 2021, MNRAS, 506, 581
Mauche C. W., Lee Y. P., Kallman T. R., 1997, ApJ, 477, 832
Mikołajewska J., Zdziarski A. A., Ziółkowski J., Torres M. A. P., Casares J., 2022, ApJ, 930, 9
Miller J. M., Raymond J., Fabian A., Steeghs D., Homan J., Reynolds C., van der Klis M., Wijnands R., 2006a, Nature, 441, 953
Miller J. M. et al., 2006b, ApJ, 646, 394
Miller J. M., Raymond J., Reynolds C. S., Fabian A. C., Kallman T. R., Homan J., 2008, ApJ, 680, 1359
Motch C., Ilovaisky S. A., Chevalier C., 1982, A&A, 109, L1
Motch C., Ricketts M. J., Page C. G., Ilovaisky S. A., Chevalier C., 1983, A&A, 119, 171
Motta S. E., 2016, Astron. Nachr., 337, 398
Mudambi S. P., Maqbool B., Misra R., Hebbar S., Yadav J. S., Gudennavar S. B. S. G. B., 2020, ApJ, 889, L17
Muñoz-Darias T., Ponti G., 2022, A&A, 664, A104
Muñoz-Darias T., Motta S., Belloni T. M., 2011, MNRAS, 410, 679
Muñoz-Darias T. et al., 2016, Nature, 534, 75
Muñoz-Darias T., Torres M. A. P., Garcia M. R., 2018, MNRAS, 479, 3987
Muñoz-Darias T. et al., 2019, ApJ, 879, L4
Neilsen J., Lee J. C., 2009, Nature, 458, 481
Novikov I. D., Thorne K. S., 1973, in DeWitt C., DeWitt B., eds, Black Holes (Les Astres Occlus). Gordon and Breach, New York, p. 343
Özbey Arabacı M., Kalemci E., Dinçer T., Bailyn C. D., Altamirano D., Ak T., 2022, MNRAS, 514, 3894
Paice J. A. et al., 2021, MNRAS, 505, 3452
Ponti G., Fender R. P., Begelman M. C., Dunn R. J. H., Neilsen J., Coriat M., 2012, MNRAS, 422, L11
Ponti G., Muñoz-Darias T., Fender R. P., 2014, MNRAS, 444, 1829
Ponti G., Bianchi S., Muñoz-Darias T., De K., Fender R., Merloni A., 2016, Astron. Nachr., 337, 512
Postma J. E., Leahy D., 2017, PASP, 129, 115002
Remillard R. A., McClintock J. E., 2006, ARA&A, 44, 49
Russell D. M., Miller-Jones J. C. A., Maccarone T. J., Yang Y. J., Fender R. P., Lewis F., 2011, ApJ, 739, L19
Sánchez-Sierras J., Muñoz-Darias T., 2020, A&A, 640, L3
Schenker K., King A. R., Kolb U., Wynn G. A., Zhang Z., 2002, MNRAS, 337, 1105
Schlafly E. F., Finkbeiner D. P., 2011, ApJ, 737, 103
Schnittman J. D., Homan J., Miller J. M., 2006, ApJ, 642, 420
Shakura N., Sunyaev R., 1973, A&A, 24, 337
Shimura T., Takahara F., 1995, ApJ, 440, 610
Stella L., Vietri M., 1998, ApJ, 492, L59
Stella L., Vietri M., Morsink S. M., 1999, ApJ, 524, L63
Stiele H., Kong A. K. H., 2020, ApJ, 889, 142
Summons D. P., Arévalo P., McHardy I. M., Uttley P., Bhaskar A., 2007, MNRAS, 378, 649
Tagger M., Pellat R., 1999, A&A, 349, 1003
Tandon S. et al., 2017, AJ, 154, 128
Tandon S. et al., 2020, AJ, 159, 158
Tetarenko B. E., Dubus G., Lasota J. P., Heinke C. O., Sivakoff G. R., 2018a, MNRAS, 480, 2
Tetarenko A. J., Petitpas G., Sivakoff G. R., Miller-Jones J. C. A., Russell T. D., Schieven G., Jacpot Xrb Collaboration, 2018b, Astron. Telegram, 11831, 1
Tetarenko B. E., Shaw A. W., Manrow E. R., Charles P. A., Miller J. M., Russell T. D., Tetarenko A. J., 2021a, MNRAS, 501, 3406
Tetarenko A. J. et al., 2021b, MNRAS, 504, 3862
Thomas J. K. et al., 2022, MNRAS, 513, L35
Titarchuk L., Fiorito R., 2004, ApJ, 612, 988
Torres M. A. P., Casares J., Jiménez-Ibarra F., Álvarez-Hernández A., Muñoz-Darias T., Armas Padilla M., Jonker P. G., Heida M., 2020, ApJ, 893, L37
Tucker M. A. et al., 2018, ApJ, 867, L9
van der Klis M., 1989, in Ögelman H., van den Heuvel E. P. J., eds, NATO Advanced Study Institute (ASI) Series C, Vol. 262, Timing Neutron Stars. Kluwer Academic Publishers, Dordrecht,p. 27
van der Klis M., 1997, in Maoz D., Sternberg A., Leibowitz E. M., eds, Astrophysics and Space Science Library, Vol. 218, Astronomical Time Series. Kluwer Academic Publishers,Dordrecht,p.121
van der Walt S., Colbert S. C., Varoquaux G., 2011, Comput. Sci. Eng., 13, 22
van Paradijs J., 1996, ApJ, 464, L139
van Paradijs J., McClintock J. E., 1994, A&A, 290, 133
Varnière P., Rodriguez J., Tagger M., 2002, A&A, 387, 497
Varnière P., Tagger M., Rodriguez J., 2012, A&A, 545, A40
Vaughan S., 2005, A&A, 431, 391
Vaughan S., Edelson R., Warwick R. S., Uttley P., 2003, MNRAS, 345, 1271
Veledina A., Poutanen J., 2015, MNRAS, 448, 939
Veledina A., Poutanen J., Vurm I., 2013, MNRAS, 430, 3196
Vernet J. et al., 2011, A&A, 536, A105
Virtanen P. et al., 2020, Nat. Methods, 17, 261
Woodgate B. E. et al., 1998, PASP, 110, 1183
Yoshitake T. et al., 2022, PASJ, 74, 805
Yu W., Zhang J., Yan Z., Wang X., Bai J., 2018, Astron. Telegram, 11510, 1
Zdziarski A. A., Gierliński M., 2004, Prog. Theor. Phys. Suppl., 155, 99
Zhao X. et al., 2021, ApJ, 916, 108

This paper has been typeset from a TEX/LATEX file prepared by the author.